Carbon 230 (2024) 119623

Contents lists available at ScienceDirect

Carbon

journal homepage: www.elsevier.com/locate/carbon

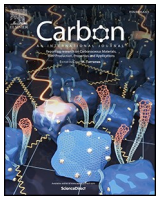

Controlling the optoelectronic properties of nitrogen-doped carbon quantum dots using biomass-derived precursors in a continuous flow system

Kiem G. Nguyen [a], Matej Huš [b,c,d], Ioan-Alexandru Baragau [a,e], Elisa Puccinelli [a], James Bowen [f], Tobias Heil [g], Adela Nicolaev [e], Deborah Andrews [a], Muhammad Tariq Sajjad [a], Steve Dunn [a], Suela Kellici [a,*,1]

[a] School of Engineering, London South Bank University, 103 Borough Road, London, United Kingdom
[b] National Institute of Chemistry, Department of Catalysis and Chemical Reaction Engineering, Hajdrihova 19, SI-1000, Ljubljana, Slovenia
[c] Association for Technical Culture of Slovenia (ZOTKS), Založka 65, SI-1000, Ljubljana, Slovenia
[d] Institute for the Protection of Cultural Heritage of Slovenia (ZVKDS), Research Institute, Poljanska 40, SI-1000, Ljubljana, Slovenia
[e] National Institute of Materials Physics, Atomistilor 405A, 077125, Magurele, Ilfov, Romania
[f] School of Engineering and Innovation, The Open University, Walton Hall, Milton Keynes, MK7 6AA, United Kingdom
[g] Max Planck Institute for Solid State Research, 70569, Stuttgart, Germany

A B S T R A C T

The synthesis of carbon quantum dots (CQDs) from high molecular weight biomass-derived precursors poses a significant challenge due to the complex molecular structures and low conversion efficiency. This work demonstrates a green, rapid, and sustainable continuous hydrothermal flow synthesis (CHFS) approach for nitrogen-doped carbon quantum dots (NCQDs) from various biomass-derived precursors, including high molecular weight polymeric sources like chitosan, lignin, and humic acid. We find that the precursor structure significantly impacts the size of the fabricated NCQDs and their optical properties. Citric acid, a low molecular weight precursor, yields NCQDs with excitation-independent emission, higher quantum yields, and low non-radiative losses, while NCQDs derived from polymeric precursors exhibit excitation-dependent, red-shifted, and lower efficiency emission. Theoretical calculations, performed to understand the configuration and distribution of nitrogen dopants within the NCQD structure, show that pyridinic and graphitic nitrogen atoms exhibit a strong preference to aggregate near the centre of the edge of the NCQD and not in the vertices nor in the graphitic core, thus affecting the HOMO and LUMO, bandgap, and light absorption and emission wavelengths. The life cycle assessment (LCA) analysis highlights the green and scalable advantages of the CHFS process for producing NCQDs compared to batch methods, making it a sustainable and economically viable approach for large-scale NCQD synthesis from high molecular weight biomass-derived precursors. Hence, the combination of experimental data and theoretical calculations provides a comprehensive understanding of the structure-property relationships in these NCQDs.

1. Introduction

Considerable research efforts have focused on developing and optimizing methods to synthesise carbon quantum dots (CQDs) with precise control over properties such as particle size, surface chemistry, and photoluminescence emission [1]. Various sustainable carbon sources, from small organic molecules to polymers and biomass, have been utilised to achieve CQDs with high quantum yields and desired functionalities [2,3]. These include citric acid, lignin, chitosan, and humic acid, which are all derived from renewable resources.

Citric acid, a readily abundant, low-cost carbon source, has a high carbon content due to its the central backbone and carboxyl groups. This versatility makes it suitable for a variety of surface functionalization [4]. Biopolymers like chitosan as well as biomaterials like humic acid and lignin have also shown promise as CQD precursors. Lignin is an abundant natural polymer in plant cell walls that is, currently, underutilized as a sustainable precursor for activated carbons. Extracting value from lignin waste streams from pulping and biorefineries could provide environmental and economic benefits [2]. Chitosan, a nitrogen rich natural polysaccharide derived from chitin, has unique properties for biomedical and environmental applications. Converting chitosan into CQDs expands its potential uses [5]. Humic acid, widely found in soils, peat, brown coals, and natural waters, possesses carboxylic, phenolic, and other oxygen-rich functional groups which are useful for

* Corresponding author.
E-mail address: kellicis@lsbu.ac.uk (S. Kellici).
[1] http://www.nano2d.co.uk.

https://doi.org/10.1016/j.carbon.2024.119623
Received 24 April 2024; Received in revised form 7 September 2024; Accepted 9 September 2024
Available online 12 September 2024

synthesizing carbon-based nanomaterials [6]. These high molecular weight precursors from natural resources offer sustainable routes to low-cost, scalable CQD production. They provide abundant surface functional groups for facile surface passivation and doping. However, challenges remain in controlling CQD size distribution, functionalities and doping, and preventing aggregation [7].

Continuous hydrothermal flow synthesis (CHFS) has emerged as a promising approach. It offers precise control over materials properties through tunability of reaction parameters such as temperature, pressure, and residence time [8]. The CHFS process is environmentally friendly and scalable, with economic advantages in synthesizing nanomaterials [9]. CHFS enables continuous production without batch-to-batch variability. The process provides rapid heating and quenching cycles to promote carbonization and activation reactions from carbon precursors in a controlled manner [10]. The temperature and pressure of supercritical water break down the precursor structure allowing it to repolymerize into novel carbon materials. This allows better control and tuning of carbon products compared to conventional techniques resulting in uniform CQDs nanoparticles. Unlike conventional carbonization techniques like pyrolysis that tend to destroy aromatic structures, CHFS better preserves the ring-like arrangements in precursors [11]. In CHFS systems, the hydrolysis and polycondensation of reactive groups under supercritical water temperatures promote self-assembly of carbon core networks [12]. We previously reported the mechanism of carbon nanoparticle nucleation using various nitrogen-containing precursors [13]. Nitrogen doping, while extensively studied, remains an important step for enhancing the optical properties of carbon quantum dots, and consequently, their applications [14]. The source of nitrogen leads to differences in doping levels and the nature of nitrogen incorporation (substitutional, interstitial, or surface doping), as well as particle size. Furthermore, the carbon source is important because it serves as the fundamental building block for the formation of CQDs and can significantly influence the size, structure, and surface properties of the resulting CQDs. This, in turn, can affect the efficiency of nitrogen doping and the overall optical properties of NCQDs.

In this work, we provide new insights into NCQDs formation mechanisms using varied carbon sources via CHFS. By processing under the same continuous hydrothermal carbonization conditions, we track how structure and composition of four precursors, lignosulfonic acid sodium salt, chitosan, humic acid sodium salt and citric acid, impact the optical, physical, chemical, and morphological properties of the as produced NCQDs. To understand the impact of varying carbon sources, we relate the effects of nanoparticle size on the electronic properties and reactivity to the distribution of nitrogen atoms as determined by ab initio calculations. First-principles calculations were performed at the hybrid level to understand the influence of nitrogen on carbon quantum dots. In particular, we evaluated their reactivity, energetics associated with the most favourable sites for N-doping, and the effects on the electronic structure.

A Life Cycle Assessment (LCA) was conducted to evaluate the potential environmental implications of utilizing CHFS for NCQDs production. This study compared the environmental impact of CHFS with batch hydrothermal synthesis, emphasizing green chemistry principles. By focusing on the use of supercritical water and biomass-derived precursors, the LCA highlights CHFS's role in enhancing the sustainability of high-quality quantum dots (NCQDs) production [15].

2. Experimental methodology and characterisation

2.1. Materials

Lignosulfonic acid sodium salt - $C_{20}H_{26}O_{10}S_2.2Na$ (average Mw ~52,000, average Mn ~7000), humic acid sodium salt - $C_9H_8Na_2O_4$ (technical grade), chitosan low molecular weight - $C_{56}H_{103}N_9O_{39}$ (technical grade), and citric acid - $C_6H_8O_7$ (99.5 %) were purchased from Sigma-Aldrich (UK). Urea - CH_4N_2O (99 %) was purchased from Fisher Chemical (U.K). These were used as received without further modification. Deionized water (15 MΩ) from an ELGA Purelab system was used for all the experiments.

2.2. The synthetic methodology of producing NCQDs

Fig. 1 presents a schematic of the CHFS system employed in this study. Pump 1 (P1) delivered deionized water. Both Pump 2 (P2) and Pump 3 (P3) were used to deliver the carbon and nitrogen precursors. The carbon precursor was a 70.0 mg mL^{-1} aqueous solution of either lignosulfonic acid sodium salt, chitosan, humic acid, or citric acid. The nitrogen precursor was a 1.0 M solution of urea. A back pressure regulator (BPR) maintained the system pressure at 24.8 MPa.

The deionized water flowed through a 450 °C heater to reach a supercritical state. The carbon and nitrogen precursors were mixed at room temperature via a T-junction. The nitrogen-doped carbon quantum dots (NCQDs) were synthesised in a counter-current flow reactor where the supercritical water flowed against the mixture of carbon and nitrogen. The flow rates of 20 mL min^{-1} (P1), 10 mL min^{-1} (P2), and 10 mL min^{-1} (P3) controlled the 1.6 s reaction time. The NCQDs in suspension were collected and cleaned with a molecular weight cut-off membrane of 30 kD, and denoted as NCQDs-Lignin, NCQDs-Chitosan, NCQDs-Humic and NCQDs-Citric.

2.3. Characterisation

High-resolution transmission electron microscopy (HRTEM) was utilised to investigate the morphology of the as-synthesised NCQDs, using a double-corrected, FEG JEOL ARM200F microscope. The prepared NCQDs solution (1.0 mL) was diluted in ethanol (9.0 mL), deposited onto a holey carbon-coated Cu-grid (400 μm), and allowed to dry under room temperature conditions. The HRTEM images were collected using an acceleration voltage of either 60 kV or 200 kV. Image analysis was conducted using ImageJ software.

Atomic force microscopy (AFM) was performed with an Asylum Research MFP-3D, operating in tapping mode and using Nano-sensors PPP-NCL probes. The samples for AFM measurements were prepared by depositing the NCQDs suspensions onto mica substrates and dried under laboratory conditions. AFM image processing included plane correction and scar removal using the built-in functions of the software.

The FTIR spectra of the freeze-dried NCQDs samples were recorded using a Shimadzu IRAffinity-1S Fourier transform infrared spectrophotometer. Measurements were taken between 500 and 4000 cm^{-1} using an external beam with scans set to 100 at a resolution of 8.

Raman spectra were measured with a Horiba LabRAM HR Evolution spectrometer with radiation at 633 nm. The samples for Raman measurements were prepared by depositing the synthesised NCQDs suspensions onto SERS-silver. Measurements were conducted in the range of 800–2000 cm^{-1}, with 50 % laser power.

X-ray diffraction (XRD) patterns of the synthesised NCQDs were obtained using a Bruker D8 Advance powder X-ray diffractometer equipped with a Cu Kα radiation source.

X-ray photoelectron spectroscopy (XPS) analysis was performed in an AXIS Ultra DLD (Kratos Surface Analysis) system using Mg Kα (1253.6 eV) radiation produced by a non-monochromatized X-ray source at an operating power of 144 W (12 kV × 12 mA). The samples for XPS measurement were prepared by depositing the NCQDs suspensions on a silver substrate. Then, the deposited NCQDs/silver substrate was placed in a vacuum oven (80 °C) for 60 min.

UV–Vis absorbance spectra were recorded using a Shimadzu UV-1800. Measurements were taken in the range of 200–800 nm with a 10 mm quartz cuvette containing a suspension of NCQDs. The sample for UV–Vis measurements was prepared by diluting 1.0 mL of NCQDs into 50.0 mL of de-ionized water.

Photoluminescence (PL) spectroscopy was measured with a Shimadzu RF-6000 fluorophotometer. The emission spectra were recorded

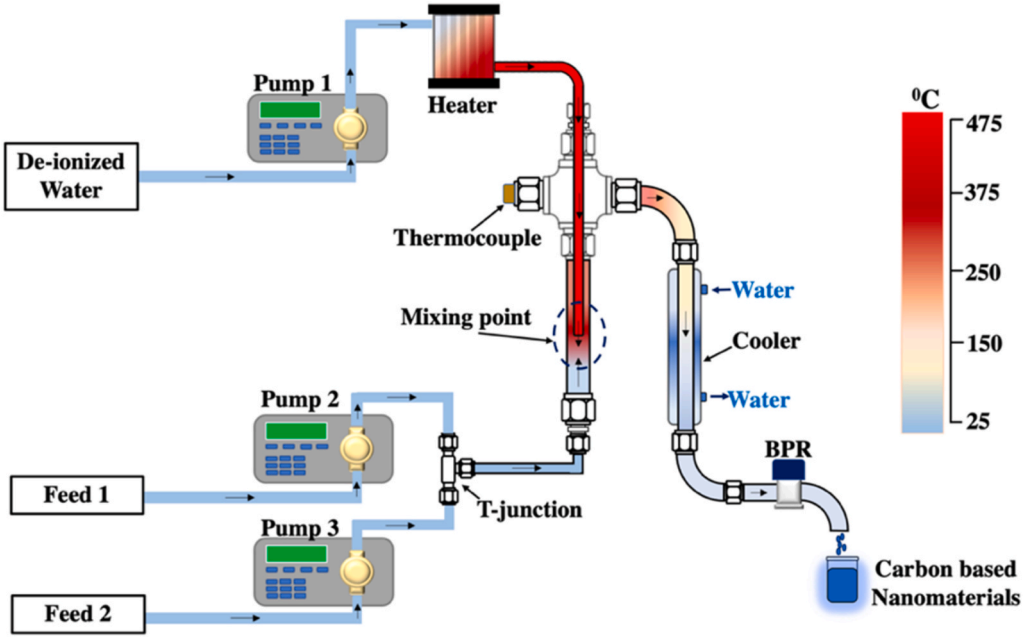

Fig. 1. The continuous hydrothermal flow synthesis process used for the synthesis of nitrogen-doped carbon quantum dots from either lignosulfonic acid sodium salt, chitosan, humic acid, or citric acid, with urea serving as the nitrogen precursor.

using an excitation wavelength of 300 nm–520 nm with a step size of 20 nm. For PL measurements, the original solution of as-synthesised NCQDs was diluted using deionized water to achieve optimized optical density solutions of 0.1 OD (optical density units) at each excitation wavelength. An Edinburgh Instrument, FLS1000 Photoluminescence spectrometer, was used to measure the PL lifetime and the quantum yield (PLQY) of the samples. The PL lifetime was measured using a 375 nm pulsed picosecond laser. The data was fitted with 3-exponentials after deconvolution with the instrument response function. The PLQY of the samples was measured using an integrating sphere by exciting the samples with a xenon lamp.

Ultraviolet photoemission spectroscopy (UPS) measurements were performed using a He I (21.2 eV) radiation source fitted in a Thermo NEXSA with a bias of −9 V, allowing extraction of the work function (Φ). The work function of the synthesised NCQDs was computed using the following equation: $\Phi = h\nu - E_k$ (Eq. (1)) where: Φ is the work function, h is Planck's constant, ν is the photon frequency, and E_k is the kinetic energy of the emitted photoelectrons [16].

2.4. Theoretical calculations

Additional insight into the structure of the synthesised NCQDs was obtained from extensive plane-wave density functional theory (DFT) calculations using Quantum ESPRESSO 7.2 [17,18]. The structures were geometrically optimized at the PBE level. The electronic properties of the smaller structures were calculated at Heyd-Scuseria-Ernzerhof (HSE) level, using the projector augmented wave (PAW) pseudopotentials. The final energies were augmented with a Grimme D3 dispersion correction [19]. For isolated NCQDs, 12 Å of vacuum was introduced in each direction to avoid spurious interactions across adjacent cells and gamma point sampling of the reciprocal space sufficed. Graphene (limit case of an infinite structure) was sampled with a 4 × 4 × 4 K-point mesh. The kinetic energy cut-off for wave functions and charge density of 40 Ry and 350 Ry, respectively, were used. A Gaussian smearing for Brillouin-Zone integration of 0.003 Ry was used to speed up convergence. Different sized NCQDs were compared (C16, C24, C32, C42, C78, C114, C116, C138) to ascertain trends in bandgap and HOMO/LUMO position with respect to core carbon size, as shown in Fig. 2. The effects of nitrogen-doping were probed on the C116 structure as a compromise between the high computational demands, which increases quadratically with size of structure, and similarity to a realistic sample. Moreover, the structure had to be sufficiently large to accommodate enough different positions of the nitrogen atoms for comparison.

The infrared (IR) spectra calculations were conducted at the hybrid level, utilizing the long-range corrected hybrid functional wB97XD with an empirical dispersion correction, as implemented in Gaussian 16 [20]. The 6-31G** basis set was employed, which has a scaling factor of 1.000 for reproducing IR spectra, as listed in the NIST database. As will be elaborated later, the IR spectra were computed on a representative model compound for NCQD (C32). This was accomplished using the Linear Combination of Atomic Orbitals (LCAO) approach, due to the significant computational cost associated with phonon calculations of large systems in the plane-wave approach. These calculated IR spectra facilitated a comparative analysis of trends among differently decorated NCQDs.

2.5. Life cycle inventory (LCI) and Life Cycle Impact Assessment (LCIA)

The Life Cycle Inventory (LCI) assessment, conducted to evaluate the environmental impact of NCQDs, involved the collection of data from two primary sources. The first source of data was derived from laboratory-scale synthesis procedures. The second source was the supplementary data obtained from Ecoinvent 3.9.1, a comprehensive database extensively utilised for life cycle assessments. However, due to the inherent limitations of Ecoinvent 3.9.1, particularly in terms of inventory data availability for carbon precursors such as humic acid, chitosan, and lignin, additional inventories were constructed (as shown in Table S1-S2) using information sourced from available literature.

A cradle-to-gate LCIA was conducted, focusing on the stages from the production of precursor materials to the final product in laboratory settings. The functional unit for the LCA study is defined as the production of 1.0 mg of NCQDs. The LCI for both CHFS and Batch is provided in the supplementary information. All inputs and outputs in the life cycle inventory (LCI) are normalized to the production of 1.0 mg of NCQDs. The study utilised SimaPro software (Version 9.5.0.1) and followed the protocols of ISO14040 and ISO14044 giving a comprehensive evaluation within the specified scope of the lifecycle. The method utilised was the Environmental Footprint 3.1, Version 1.00/EF 3.1

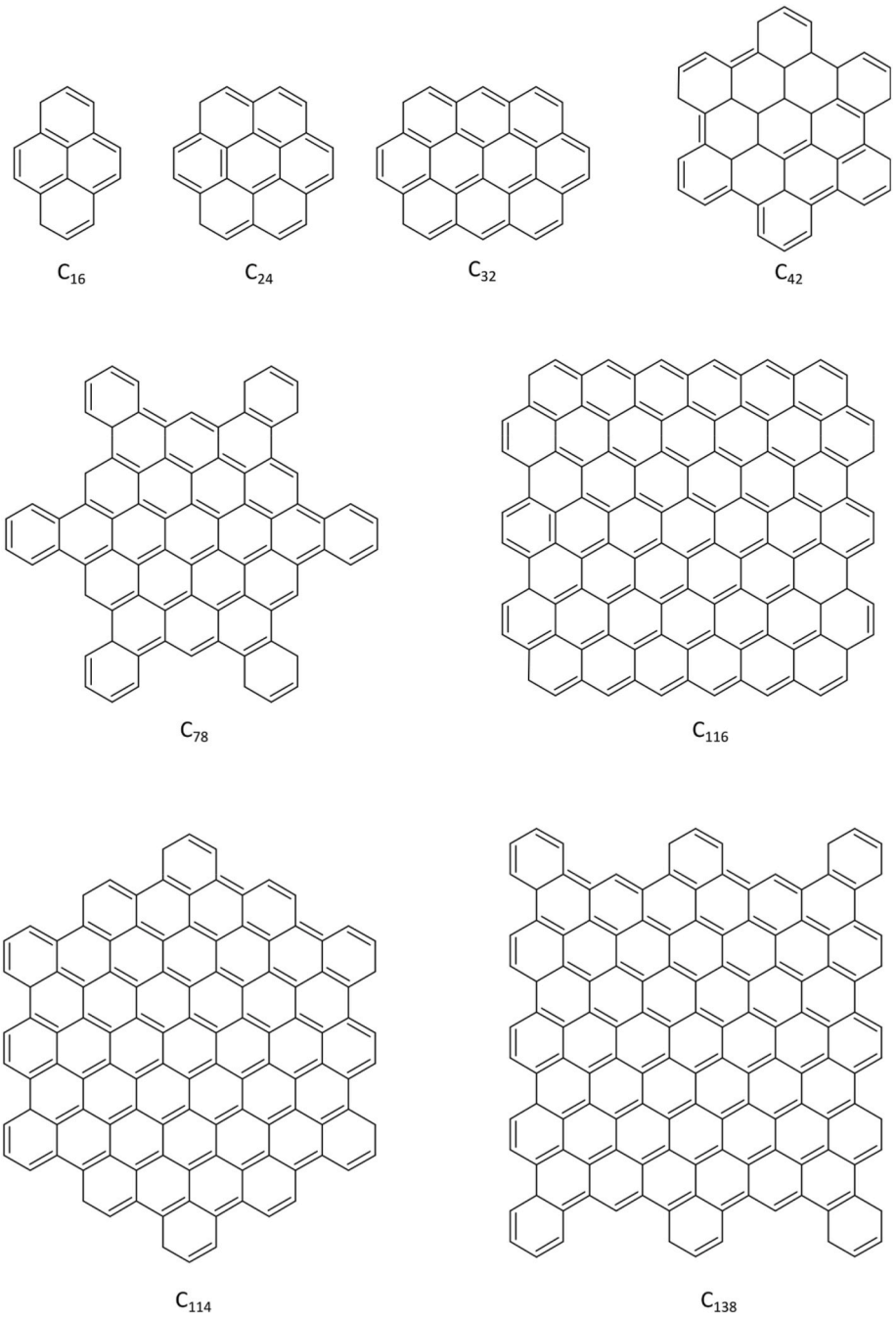

Fig. 2. Single-layered structures used for calculating the electronic properties of carbon quantum dots (CQDs).

normalization and weighting set [21].

3. Results and discussions

3.1. Morphology and chemical properties of NCQDs

The high-resolution TEM (HR-TEM) analysis shown in Fig. 3 offers insights into the morphology and graphitic carbon core structure of the synthesised NCQDs. Particle size analysis indicates a correlation between the mean NCQD diameter, and the carbon source utilised during synthesis, as summarized in Table 1. NCQDs produced from citric acid had the smallest average particle size of 3.5 nm, whereas those derived from humic acid displayed largest averaging 4.8 nm. NCQDs from lignin and humic acid demonstrated a broad particle size distribution ranging from 1.0 to 8.0 nm, whereas citric acid and chitosan yielded NCQDs within 1.0–6.0 nm size range. This variation in particle size is linked to the molecular weight and structure of the precursors [22]. Specifically, citric acid and chitosan, with their lower molecular weights lead to smaller nanoparticles [23,24]. Adiditionally, the precursor's chemical structure affects the formation of carbon nanoparticles, citric acid's simple, symmetrical structure, and chitosan's uniformity result in smaller particles with a narrower distribution. In contrast, the complex, irregular structures of lignin and humic acid produce more disordered nanoparticles with a broader size distribution [25].

NCQDs produced using citric acid show a lattice spacing of 0.21 ± 0.01 nm (Fig. S1) that corresponds with the expected (100) crystal plane of graphite-like carbon [12]. In contrast, the NCQDs synthesised with lignin, chitosan and humic acid exhibited lattice spacings of 0.31 nm, aligning with the (002) plane of more disordered graphene-like carbon [26]. Notably, chitosan-derived NCQDs also exhibited a 0.28 nm spacing

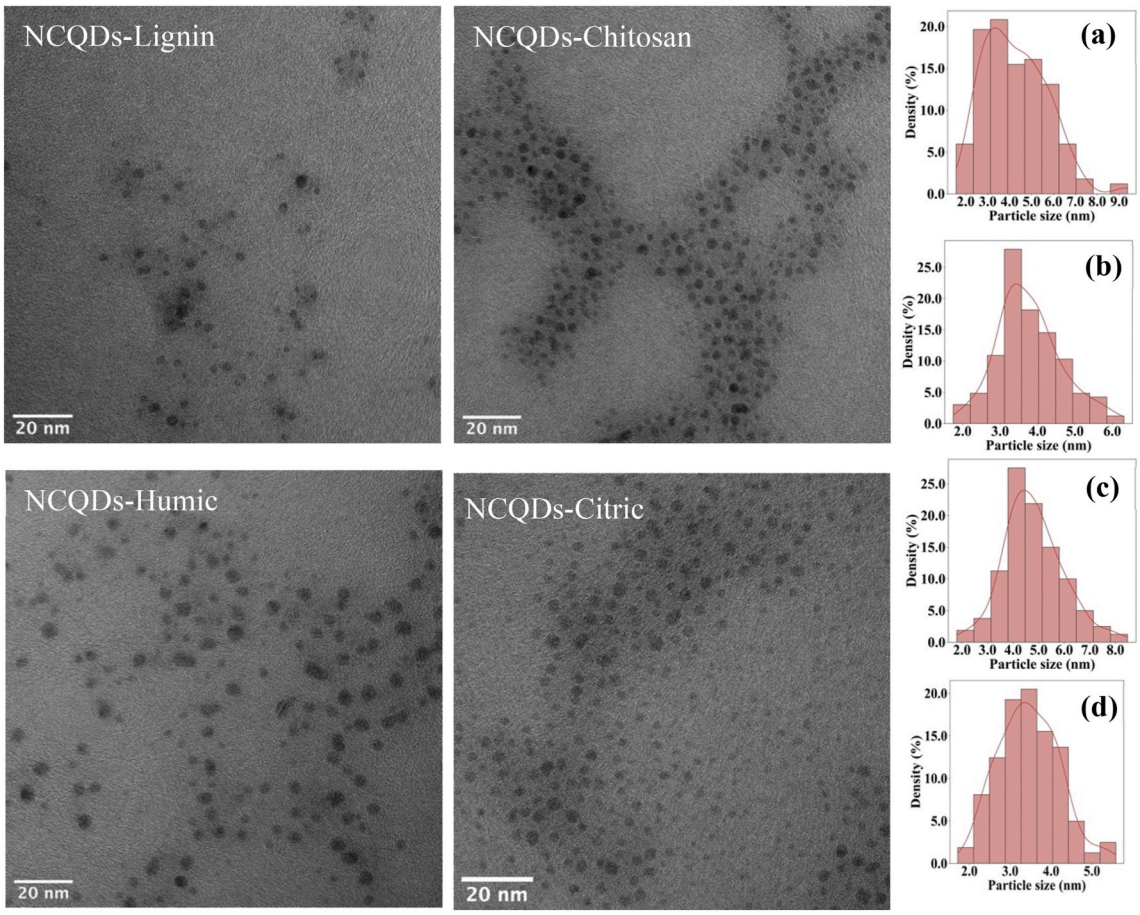

Fig. 3. HR-TEM images and particles size distribution histogram of: (a) NCQDs-Lignin, (b) NCQDs-Chitosan, (c) NCQDs-Humic and (d) NCQDs-Citric materials.

Table 1
The mean particles size and height of the synthesised NCQDs.

Sample	HR-TEM Mean Particle Size (nm)	AFM Mean Height (nm)
NCQDs-Lignin	4.3 ± 1.4	4.3 ± 0.2
NCQDs-Chitosan	3.8 ± 0.9	2.3 ± 0.2
NCQDs-Humic	4.8 ± 1.2	2.4 ± 0.3
NCQDs-Citric	3.5 ± 0.8	1.4 ± 0.2

matching the (1120) lattice plane of graphene [27]. This variation likely arises from defects and distortions introduced by the complex biomass-derived precursors [28].

To gain deeper insight into the 3D shape and structure of the as-synthesised NCQDs, atomic force microscopy (AFM) was utilised to characterize the morphology and height distribution of the synthesised NCQDs, as shown in Figure S1 (a-d). The results revealed that the NCQD heights ranged from 1.4 nm to 4.3 nm depending on the precursor material (Table 1). NCQDs produced from citric acid had the smallest height of 1.4 nm. In comparison, the use of lignin as a precursor led to larger NCQDs with heights up to 4.3 nm. The AFM image analysis supports the HRTEM results. Hence, both techniques indicating that complex, high molecular weight carbon precursors tend to produce larger NCQDs.

To determine the crystal structure of the synthesised NCQDs, X-ray powder diffraction patterns were recorded and depicted in Fig. S2. The XRD patterns of NCQDs-Citric, NCQDs-Chitosan, and NCQDs-Humic generally showed a broad peak centred around 15–30°. However, the NCQDs-Citric pattern centred around 18°, indicating the presence of some ordered layered nanocarbons with atomic structures close to graphite, corresponding to a d-spacing of 0.21 nm [29]. Meanwhile, the peaks at 2θ ≈ 20° and 25° observed in the XRD patterns of NCQDs-Chitosan and NCQDs-Humic are usually attributed to an increase in the interlayer distance in a stack of nanographene layers, with a d-spacing of approximately 0.33 nm [30]. These findings from the XRD patterns reinforce the conclusions drawn from HRTEM characterisation. The NCQDs-Lignin displayed a different XRD pattern consisting of several sharp, lower-intensity peaks located around 23.2° and 25.6°, corresponding to the (002) and (001) planes of graphitic carbon and representing the interlayer spacing of graphene sheets [31]. This observation is consistent with the HRTEM images shown in Fig. S1. Additionally, the NCQDs-Lignin showed a peak located at 28.3°, which can be attributed to the presence of residual crystalline components from the lignin precursor attached to the carbon core of the synthesised NCQDs [32].

Fourier transform infrared (FTIR) spectroscopy was utilised to characterize the functional groups in the NCQDs, as depicted in Fig. 4. All NCQD samples exhibited a broad band from 3250 to 3500 cm^{-1}, corresponding to the O–H stretch arising from carboxylic acids and alcohols as well as N–H stretches from amines and protonated amines [33]. This band was most prominent in the NCQDs derived from chitosan and citric acid precursors. The NCQDs produced from lignin and humic acid displayed weaker bands above 3250 cm^{-1} along with an increased intensity peak around 3000 cm^{-1} attributed to C–H stretching of alkyl groups [34]. The presence of these nitrogen containing functional groups confirms successful N-doping of the carbon quantum dots. The relative intensities of O–H/N–H and C–H bands demonstrate that different precursors can influence the surface chemistry of NCQDs. A peak at 1600 cm^{-1} was observed in the FTIR spectra of the synthesised NCQDs, corresponding to the stretching vibration of C═C double bonds [35]. The fingerprint region showed a peak at 1450 cm^{-1} arising from

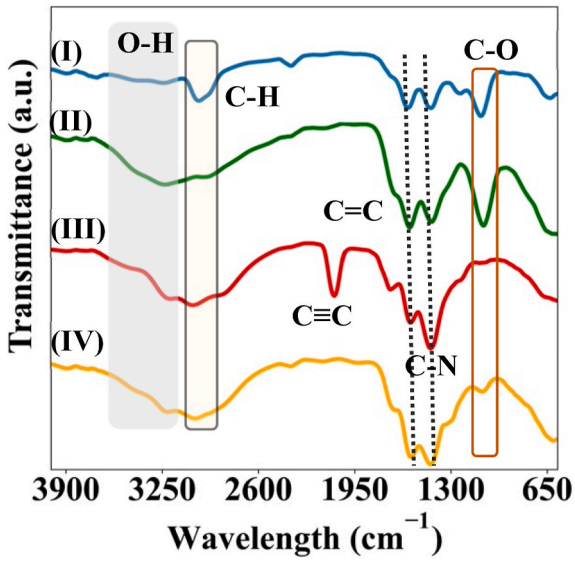

Fig. 4. Fourier transform infrared spectra of: (I) NCQDs-Lignin, (II) NCQDs-Chitosan, (III) NCQDs-Humic, (IV) NCQDs-Citric.

C–N single bond stretches, confirming the incorporation of nitrogen-containing groups.

Our experimental findings compare favourably with the theoretically calculated spectra, shown in Fig. 5. We observe a characteristic peak around 3220 cm^{-1}, corresponding to C–H stretch and C═C double bonds cause a peak at 1600 cm^{-1}. Nitrogen doping induces a strong peak at 1450 cm^{-1} due to graphitic nitrogen. Pyrrole motifs are recognised by the characteristic N–H stretch around 3700 cm^{-1}, while the protonated pyridinic N–H bond vibrates at 3620 cm^{-1} and NH_2 has two peaks at 3730 and 3620 cm^{-1}. A distinguishing peak at 1100 cm^{-1} associated with C–O bond stretches was observed for NCQDs produced from lignin and chitosan precursors [36]. In contrast, this C–O stretch peak was minimal to non-existent in the NCQDs derived from humic acid and citric acid. The presence and intensity variations for the C–O vibrations suggest differing oxygen contents among the NCQDs that relates to carbon precursors. Interestingly, a peak at 2080 cm^{-1}, attributable to C ≡ C triple bonds, was uniquely observed in the FTIR spectrum of the synthesised NCQDs-Humic, and this distinction peak can be related to the hydrothermal decomposition of humic substances potentially producing unsaturated carbon bonds [37]. Analysis of the Raman spectra (Fig. 6) provided additional insights into the structure of the NCQDs. All samples displayed the expected D and G bands stemming from the graphitic carbon framework.

The G band at approximately 1580 cm^{-1} corresponds to the E_{2g} vibrational mode of sp^2 hybridized carbon, confirming the presence of graphitic domains within the NCQDs. The D band at 1350 cm^{-1} is associated with structural defects and discontinuities in the carbon lattice [38]. The NCQDs produced from citric acid and urea exhibited lower I_D/I_G band intensity ratios (Fig. 6b) compared to the other samples. This shows that the NCQDs-Citric possess higher quality graphitic carbon with less defects. In contrast, NCQDs synthesised using high molecular weight precursors like lignin and humic acid exhibited greater D band intensity relative to the G band. The heightened D band suggests more numerous defects are present in the NCQD carbon structure formed from these biomass-derived sources [39]. The deconvoluted Raman spectra (Fig. S3) of the synthesised NCQDs reveal additional peaks: the D* band located around 1200 cm^{-1} and the D′ band located around 1600 cm^{-1}. The D* band is associated with the breathing modes of sp^2 rings and can indicate the presence of amorphous carbon structures. The D′ band is attributed to defects in the graphitic lattice providing information about the degree of disorder in the carbon structure [40]. The computed A_D/A_G ratios confirm the trends observed in the I_D/I_G ratios. These results reveal that the synthesised NCQDs-Citric possesses the lowest A_D/A_G ratio of 0.17, indicating a higher degree of C sp^2. In contrast, the NCQDs-Humic acid showed the highest A_D/A_G ratio of 2.97, suggesting a more disordered carbon structure with a higher proportion of defects and amorphous regions [41]. These findings from Raman analysis are aligned to the HRTEM images of the synthesised NCQDs.

X-ray photoelectron spectroscopy (XPS) analysis was performed to determine the chemical composition of the NCQDs. The core level spectra were deconvoluted using Voigt functions, incorporating Lorentzian and Gaussian line widths along with distinct inelastic backgrounds for each component. The minimum number of fitting components was used to optimise the spectral fits. The survey scan XPS spectra revealed three typical peaks, attributed to C1s at 285 eV, O1s at 531 eV, and N1s at 399 eV, providing a fingerprint of the NCQD composition [42]. Analysis of the relative elemental composition, tabulated in Table S3, shows higher N content above 10 % for NCQDs

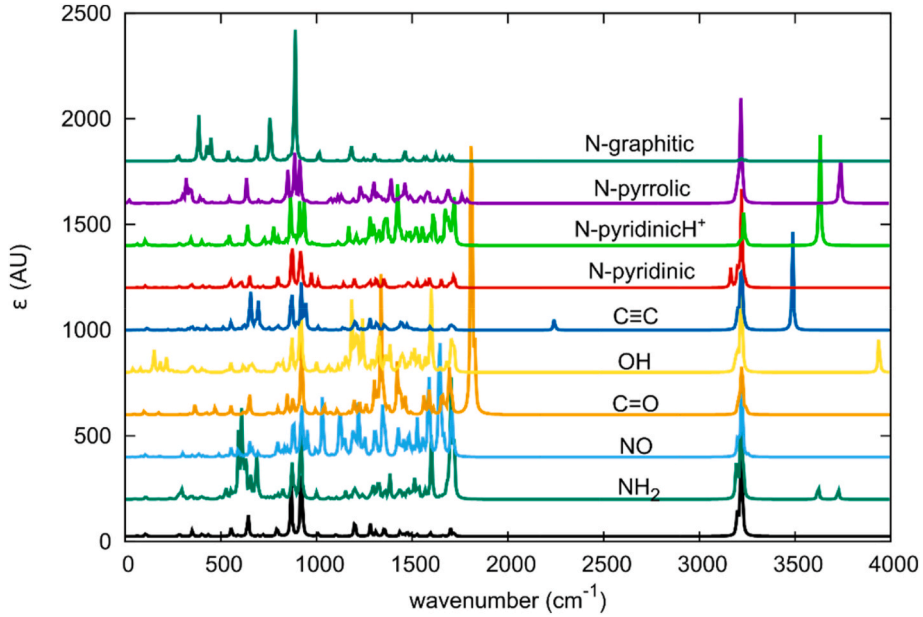

Fig. 5. Theoretically calculated IR absorption coefficients for differently decorated C_{32} structures.

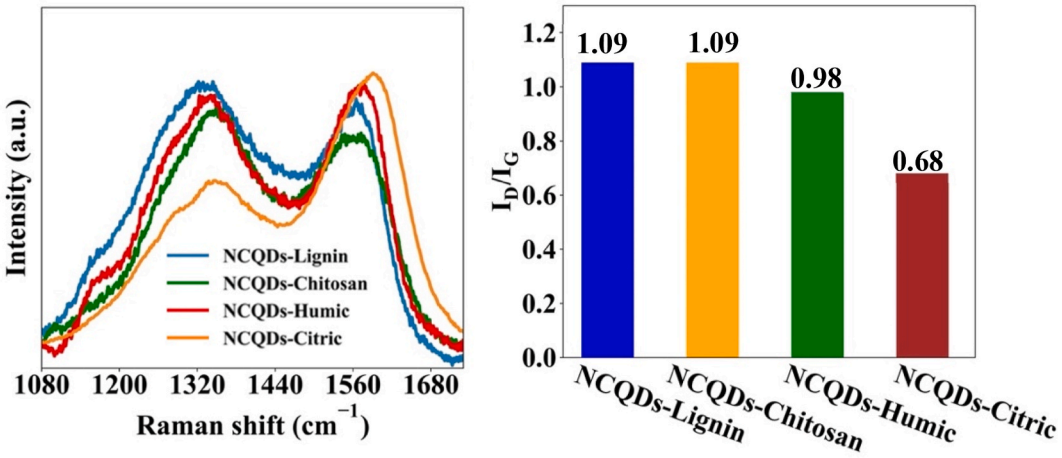

Fig. 6. (a) The Raman spectra of the synthesised NCQDs and (b) the ratio of I_D/I_G bands, located at ca. 1350 cm^{-1} and 1580 cm^{-1}.

synthesised with citric acid and chitosan precursors. In contrast, NCQDs derived from humic acid and lignin displayed a lower nitrogen incorporation 2 %. This is indicative of weaker interaction between these precursors and the N dopant sources during synthesis. In addition to low N content, the NCQDs-Humic and NCQDs-Lignin possessed higher O levels, pointing to an abundance of oxygen-rich surface defects. High resolution N1s spectra (Fig. 7) provided further insights into the nitrogen bonding environments. The NCQDs-Chitosan exhibited three N1s components at 399.5, 400.2, and 401.5 eV, assigned to pyridinic, pyrrolic, and graphitic N configurations [43]. In contrast the high resolution N1s spectra revealed the absence of pyrrolic N in the NCQDs-Humic and NCQDs-Lignin. The synthesised NCQDs-Humic exhibited pyridinic at a binding energy of 399.5 eV and graphitic nitrogen at 401.8 eV; and the synthesised NCQDs-Lignin displayed the presence of pyridinic nitrogen at 399.2 eV. The detailed N1s peak deconvolution for the as-synthesised NCQDs is summarized in Table S4. The weak fluorescence exhibited by these NCQDs correlates with the limited pyrrolic nitrogen content, which otherwise enhances photoluminescence through excited state proton transfer and surface passivation [44]. In contrast, NCQDs-Citric contained pyrrolic N (398.8 eV), along with pyridinic (396.8 eV) and protonated pyridinic N (400.4 eV). The configuration of nitrogen observed in the as-synthesised NCQDs are depicted in Fig. 7. The incorporation of pyridinic, pyrrolic, protonated pyridinic, and graphitic nitrogen within the sp^2 lattice of CQDs imparts distinct and complementary effects, enhancing their overall photoluminescent and optical properties [45]. Pyridinic nitrogen forms localized defects that introduce intermediate bandgap states, enabling lower energy photon emission to tune the fluorescence colour. Meanwhile, the pyridinic lone electron pair promotes n-type doping to improve charge transfer and electrical conductivity [46]. This can be visualised by plotting the LUMO orbital which is further discussed in the computational calculation.

Additionally, protonated pyridinic nitrogen facilitates proton transfer to further boost quantum yields while also providing positive charges to assist in surface functionalization with brighter emissive chromophores. Graphitic nitrogen directly substitutes carbon sites in the conjugated lattice, leading to bandgap reduction that allows visible light absorption and emission [47].

The visualisations of NCQDs incorporated with distinct nitrogen configuration dopant are depicted in Fig. 8.

3.2. The optical properties of NCQDs

Analysis of UV–Vis absorption data provided insights into the impact of different carbon precursors on the optical properties of the synthesised NCQDs. The absorbance was measured in a 10 mm quartz cuvette using deionized water as a reference, with the spectra for each NCQD sample shown in Fig. 9. The NCQDs derived from lignin and humic acid displayed similar broad, absorption bands extending from the UV into the visible region. This reveals their heterogeneous structure and complex optoelectronic transitions. A very broad hump centred around 285 nm likely stems from n-π* transitions of C═O bonds in the disordered NCQD Fig. 9 carbon core [48].

In contrast, the NCQDs-Citric exhibited a distinct sharp peak at 330 nm along with an absorption at 270 nm. The 330 nm absorbance band can be assigned to n-π* transitions of nitrogen or oxygen-containing surface groups [35]. Meanwhile, the 270 nm shoulder corresponds to π-π* transitions of sp^2 hybridized carbon. Unlike the other samples, chitosan synthesised NCQDs showed a broad asymmetric absorption profile spanning 270–300 nm. This wide hump arises from π-π* transitions of aromatic C═C bonds, implying formation of π-conjugated systems within the chitosan NCQD carbon core [49].

To achieve a deeper understanding about the optical properties of the NCQDs, the fluorescence emission properties of the NCQDs were investigated, the emission spectra are shown in Fig. 10. The NCQD samples displayed both excitation-independent and dependent fluorescence behaviours. The NCQDs-Citric (Fig. 10d) exhibited a rare excitation-independent emission properties, with the peak position fixed at 440 nm across all excitation wavelengths. However, the highest photoluminescence intensity occurred at 340 nm excitation, reducing significantly above 360 nm. In contrast, the NCQDs-Lignin (Fig. 10a), chitosan (Fig. 10b) and NCQDs-Humic (Fig. 10c) showed excitation-dependent emission. For NCQDs-Lignin, excitation from 280 to 400 nm resulted in increasing intensity at 510 nm emission, while longer wavelength excitation above 400 nm caused a red-shift and much weaker emission. Similarly, NCQDs-Chitosan displayed maximum 450 nm emission under 360 nm excitation, while NCQDs-Humic reached to maximum emission at 550 nm under 460 nm excitation.

To further probe the impact of different carbon precursors, the photoluminescence quantum yields (PLQY) and fluorescence lifetimes of the synthesised NCQDs were measured. The PLQY results reveal a significant effect of the carbon sources on emission capabilities. The NCQDs-Citric achieved a high 14 % PLQY, representing notable improvement over previous NCQD samples [12]. In contrast, chitosan, lignin, and humic acid – derived NCQDs showed far lower quantum yields of 4 %, <1 %, and <1 %, respectively. Fluorescence lifetime data showed that all the as-synthesised NCQDs exhibited comparable (>5ns) fluorescence lifetimes (Table S5) [50].

Analysis of the radiative and non-radiative rates indicates the biomass - derived NCQDs have higher non-radiative losses, as shown in Table S6. This arises from carbon core defects acting as non-emissive recombination centres, as observed in Raman spectra. To further investigate the effect of various the use of carbon precursors on the

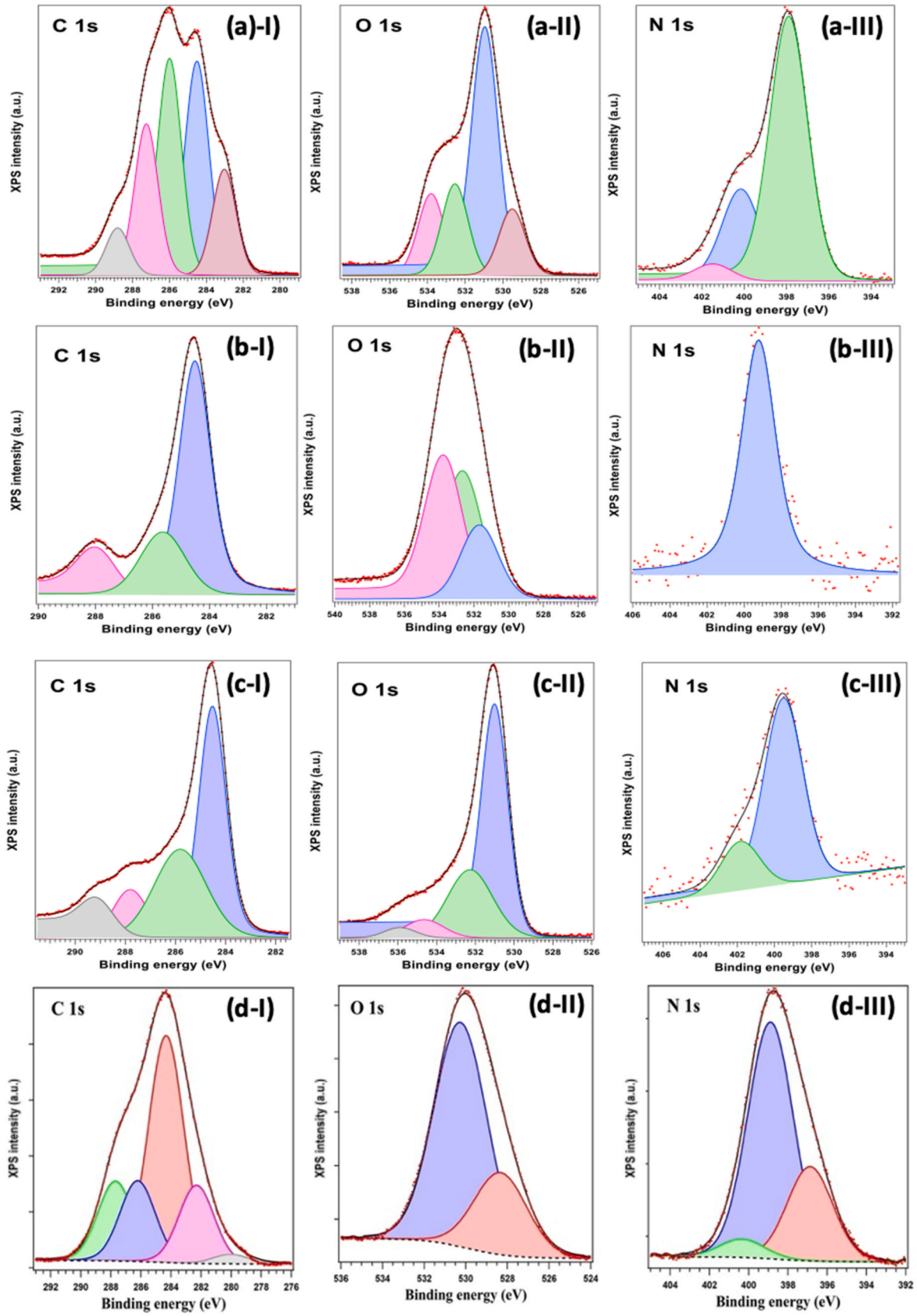

Fig. 7. The XPS spectra of the synthesised NCQDs: (a)–(I) to (a)-III NCQDs-Chitosan, (b)–(I) to (b)-(III) NCQDs-Lignin, (c)-(I)to (c)- (III) NCQDs-Humic and (d)–(I) to (d)-(III) NCQDs-Citric.

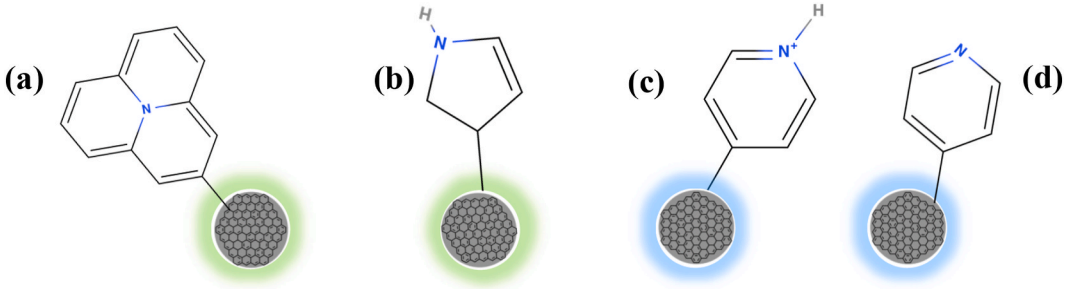

Fig. 8. The dopant configurations of nitrogen observed in the synthesised NCQDs: (a) graphitic nitrogen, (b) pyrrolic, (c) protonated pyridinic and (d) pyridinic-N.

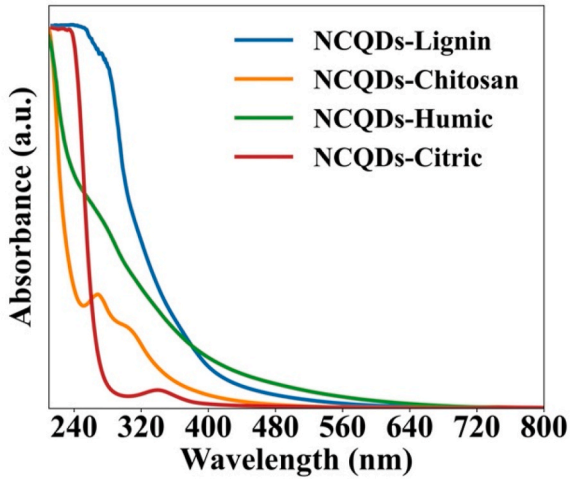

Fig. 9. The UV–Vis spectra of the synthesised NCQDs, the NCQDs-Lignin and Humic NCQDs showed a broader range of UV–Vis light absorbance.

properties of the synthesised NCQDs, ultraviolet photoelectron spectroscopy (UPS), was used to examine the electronic structure of the prepared NCQDs. The UPS spectra of the synthesised NCQDs are illustrated in Fig. 11.

UPS data analysis revealed the largest work function of 5.81 eV for NCQDs-Lignin. NCQDs-Humic and NCQDs-Chitosan showed slightly lower work functions of 5.75 eV. NCQDs-Citric exhibited the smallest work function of just 4.94 eV. The trend of higher work functions for biomass-based NCQDs aligns with their larger average particle size compared to NCQDs-Citric. According to the theoretical calculations (see Table S7), a decrease in the work function is associated with the presence of graphitic nitrogen atoms, while an increase is due to pyridinic nitrogen. Functional groups have little effect on the work function. Defects in the material, such as missing carbon atoms and the formation of triple bonds decrease the work function [51]. These finding from theoretical calculations are consistent with the finding from the FTIR data mentioned above.

The optical energy bandgap of the synthesised NCQDs were evaluated by using Tauc plot, as shown in Fig. 11c. The synthesised NCQDs-Lignin and Humic NCQDs possess bandgaps of 3.6 and 3.7 eV, NCQDs-Chitosan derived sample showed a wider 4.6eV bandgap, and NCQDs-Citric displayed the largest bandgap of 4.94 eV. Theoretical calculations show that a decrease in the bandgap is caused by graphitic nitrogen, protonated pyridine rings, and –C═O and –NO groups. The smaller bandgaps of NCQDs-Lignin and NCQDs-Humic samples can be attributed to their larger average particle sizes. The combined data from UPS and bandgap measurements provides a comprehensive picture of the synthesised NCQDs, revealing the effect of different carbon sources in tuning the energy band structures, as shown in Fig. 12.

3.3. Theoretical calculations

Carbon quantum dots were treated as finite structures of fused graphene-like rings where nitrogen doping is accounted for as various nitrogen groups and substitutions [52]. As shown in Fig. 7, these are predominantly graphitic nitrogen atoms, pyridine nitrogen atoms and their protonated forms, pyrrolic nitrogen atoms. As shown in our previous work, a compromise must be struck between the size of the investigated size and the computational cost [13]. In Table 2, the calculated bandgaps at the generalized gradient approximation (GGA) and hybrid level for differently size structures are listed. As graphene represents the limit case of a zero-bandgap material, the bandgap decreasesg as the structures grow larger in size. It is known that the GGA approaches underestimate the bandgap considerably (1–2 eV), while the hybrid functional approach is more reliable (<1 eV, typically <0.5 eV) but still slightly low. This is graphically depicted in Fig. 13, where the density of states (DOS) is shown for two representative examples (C_{16}, C_{42}) and the limit case of graphene.

3.3.1. Configurations of nitrogen doping

As nitrogen atoms are introduced in the carbon quantum dots, they can assume different sites, which cannot be distinguished in FTIR spectra. In Fig. 8, the nitrogen atoms are provisionally shown on the outer edge of the NCQDs. To ascertain if they prefer the core or the outer edge of the NCQDs, energetic calculations on the C_{116} structure were performed. All distinct carbon atoms were individually substituted for nitrogen (graphitic nitrogen). Pyridinic structures were formed in two ways: for the outer (rim) area, a conventional pyridine structure is formed by substituting a carbon atom with a nitrogen atom and removing the corresponding hydrogen atom. In the core part of the NCQD, a carbon atom is removed, and three adjacent carbon atoms are substituted for nitrogen atoms, as shown in Fig. 14. It is noted that the most favourable substitution sites (shown in blue) lie at the outer edge of the NCQD but not at the vertices, while the core is least likely to contain nitrogen defects. The energy differences are considerable. For the N-graphitic substitutions, the difference between the most and least likely site is 1.63 eV, and for the N-pyridine substitutions it is 0.97 eV. These values far exceed the accessible thermal energy (at 300 K, thermal energy is 0.025 eV) and show that the nitrogen atoms are fairly immobile and congregated at the edge. Pyrrolic rings were only evaluated at the outer edge and the differences in energy were 0.26 eV (not shown), indicating that they can form randomly.

This preferential substitution sites agree well with the reactivity of the NCQDs, which are shown in Fig. 15 as the HOMO and LUMO orbitals. Although being two-dimensional (one-layer), the carbon quantum dot is most reactive near the centre of the edge and not near the vertices. In Fig. 16, HOMO and LUMO orbitals are shown for the most common nitrogen modifications (graphitic, pyrrolic, pyridinic). It is noted that the graphitic nitrogen does not impact HOMO and LUMO, while the pyridinic and protonated pyridinic nitrogen atom strongly concentrate the LUMO orbital near the nitrogen atom, facilitating charge transfer and electrical conductivity.

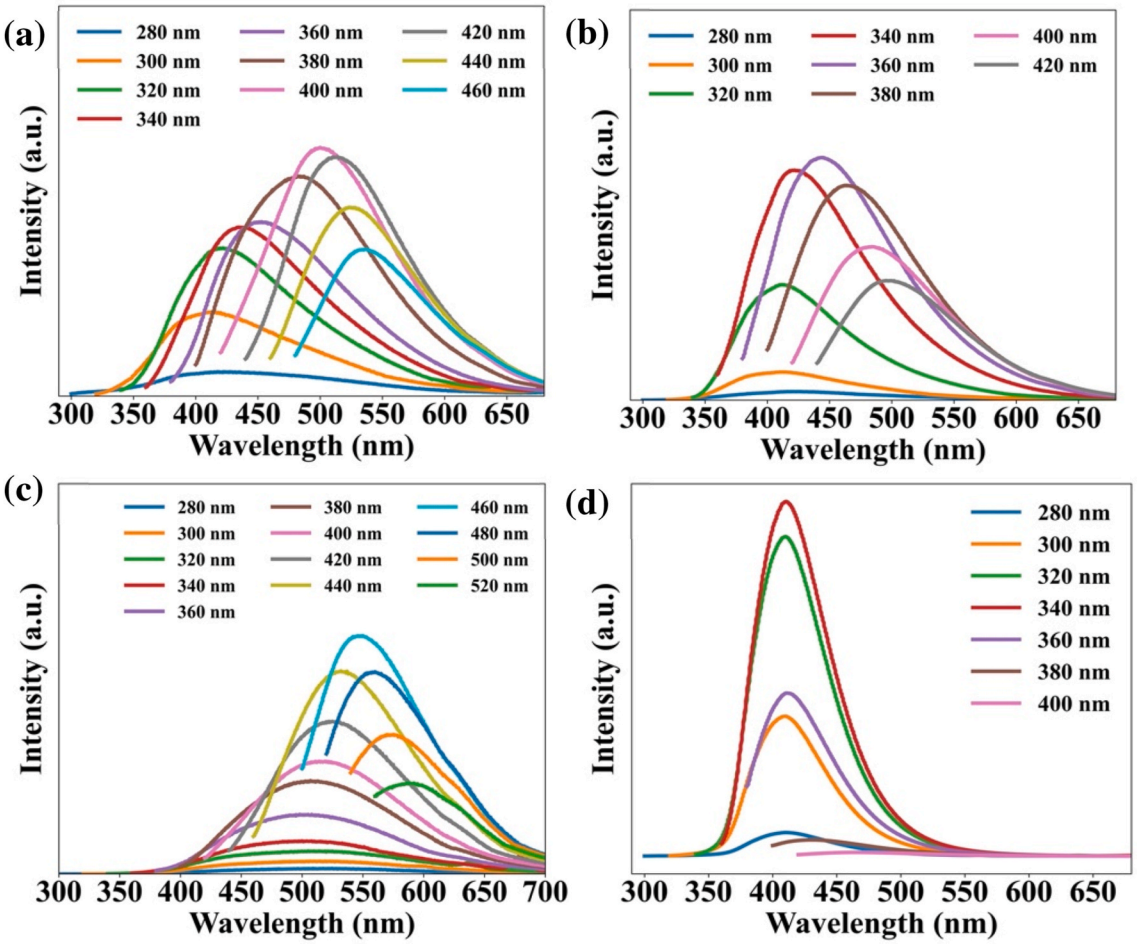

Fig. 10. The PL spectra of excitation dependent: (a)NCQDs-Lignin, (b) NCQDs-Chitosan, (c) NCQDs-Humic, and (d) NCQDs-Citric samples showing excitation - independent behaviour.

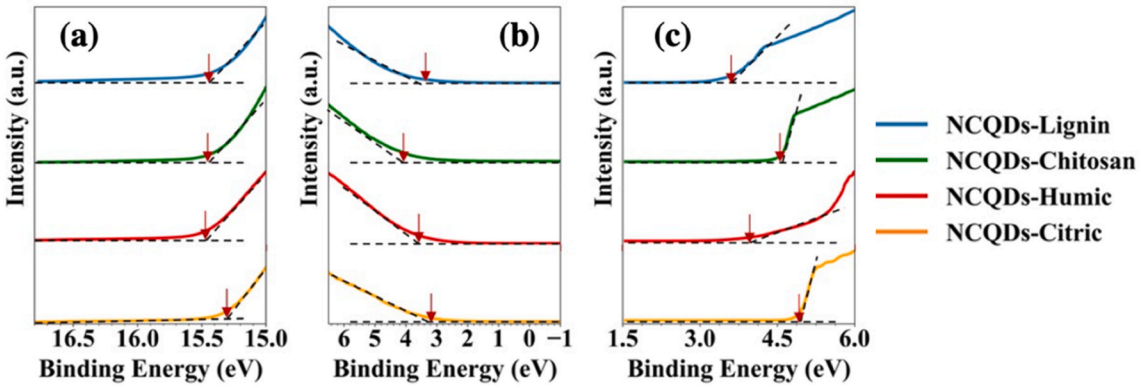

Fig. 11. The UPS spectra and Tauc plots of the synthesised NCQDs: (a) for determination of the work function, (b) valence band maximum and (c) determination of direct bandgap using Tauc plots.

3.4. Photoluminescence states of NCQDs

The photoluminescence mechanism strongly depends on the synthetic conditions and source materials [53]. Understanding these relationships provides insights into tailoring NCQDs' optoelectronic properties for different applications. In this work, synthesising NCQDs from various carbon-containing precursors, citric acid stands out for yielding NCQDs with superior optical features such as excitation-independent emission and higher quantum yields, compared to NCQDs derived from chitosan, lignin, and humic acid. This points to fundamental differences in the PL mechanism based on the carbon source. For the NCQDs synthesised from high molecular weight precursors like chitosan lignin and humic acid, the excitation-dependent behaviour and lower quantum yields indicate carbon core state emission from quantum confined conjugated π-domains [54]. Similiar effects are observed in the synthesised NCQDs-Lignin, NCQDs-Humic, and NCQDs-Chitosan samples, where larger particles sizes redshift the emission [55]. Additionally, N-graphitic is a source of red emission,

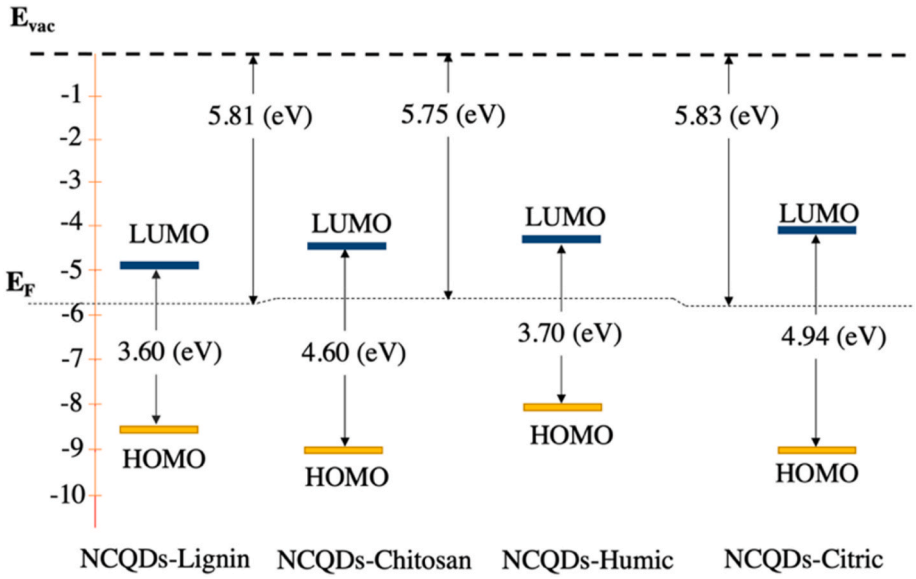

Fig. 12. The energy band structure of the synthesised NCQDs: NCQDs-Lignin and NCQDs- Humic possess narrower energy bandgap as the average particle sizes are larger.

Table 2
The calculated bandgap at the GGA (PBE) and hybrid (HSE06) levels for differently sized structures.

Structure	Bandgap (eV) – PBE	Bandgap (eV) – HSE06
C_{16}	2.63	3.38
C_{24}	2.86	3.59
C_{32}	1.92	2.60
C_{42}	2.46	3.15
C_{78}	1.98	est. 2.7[a]
C_{114}	1.52	est. 2.2[a]
C_{138}	1.30	est. 2.0[a]

[a] Estimated values.

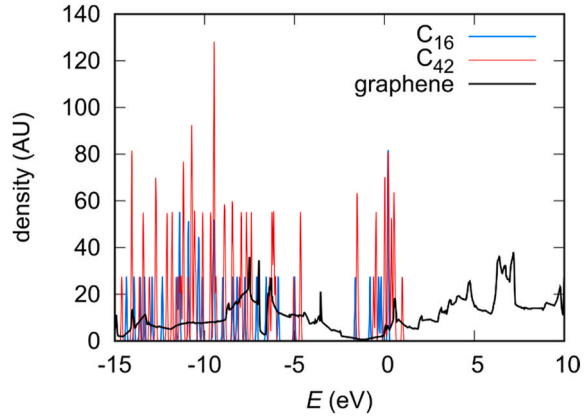

Fig. 13. *A comparison of the density of states for C_{16} and C_{42} quantum nanodots and graphene (C∞), calculated at the hybrid level (HSE06).*

which we observe only in the NCQD-Humic sample (Table S4) with a high graphitic content of 21%, potentially enhancing the overall red emission [43]. Surface defects likely allow nonradiative relaxation pathways, reducing quantum yields [56].

In contrast, citric acid-derived NCQDs exhibit excitation-independent PL and a comparable quantum yield (~14 %). Literature suggests that the reaction between citric acid and urea produces citrate-based molecular fluorophores, such as derivatives of citrazinic acid, under hydrothermal synthesis conditions through cyclization and condensation pathways [57]. [22]. Citrazinic acid displays a strong blue fluorescence which is excitation independent with the maximum excitation wavelength at $\lambda_{ex} = 340$ nm, and the maximum emission wavelength at $\lambda_{em} = 440$ nm. The UV–Vis spectrum of citrazinic acid shows a typical peak around 330 nm. The bonding of these fluorophores, whether chemically or non-covalently to the surface of NCQDs or embedded within their core, remains debatable and is certainly influenced by the local environment of the carbon dots [57]. During membrane filtration of the NCQDs, we observed some fluorescent emission in both the permeate and retentate, indicating the removal of some fluorophores not incorporated into the NCQD. In contrast, the prepared NCQDs from lignin salt, humic acid salt and chitosan lack fluorescence in the permeate after filtration, consistent with an absence of molecular fluorophores.

Previous studies found that citrazinic acid itself is not a source of stable fluorescence in water, with an 80 % decrease in photoluminescence observed after just seven days [58]. In contrast, we observed no change in photoluminescence over the same time for NCQDs-Citric. It could be suggested the sp^2-and sp^3-hybridized carbon core may act as an anchor to stabilize fluorescent structures like citrazinic acid over time. However, scientific reports also indicate that the formation of these species depends on reaction conditions, including time and temperature [57] with decompostion temperatures reported to be around 200-300 °C. In contrast, our CHFS systems operates under supercritical conditions. The relationship between fluorescent molecules generation and the evolving carbon nanoparticle matrix during synthesis is indeed complex and requires further investigation. Optimizing the incorporation of molecular fluorophores versus carbonized domains lays the foundation for producing the next generation of NCQDs with controlled optical properties for diverse emitter applications.

3.5. Life Cycle Impact Assessment

The results of the Life Cycle Impact Assessment (LCIA) presented in Fig. 17 illustrate the environmental impacts of producing NCQDs using with various carbon precursors. These impacts are shown across different categories and are measured in micro points (Eco Points). The unit used in SimaPro for this measurement is called Eco-point (Pt), chosen for its ability to effectively aggregate the outcomes of key impact categories into a single score. A value of 1 Pt represents 1/1000 of the annual environmental impact of an average European [59].

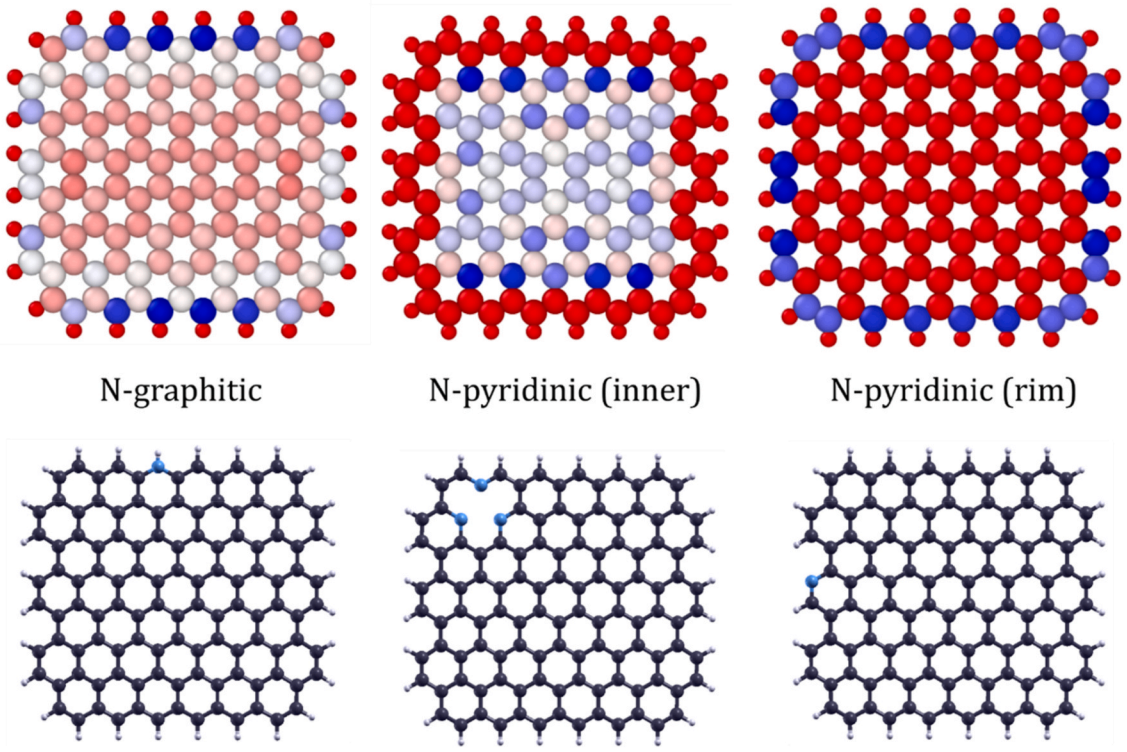

Fig. 14. (top) Relative energy of nitrogen substitution (graphitic or pyridinic) in the C_{116} structure. Colour code: deep blue 0.00 eV (most likely), deep red 2.00 eV (least likely). (bottom): The most stable structures.

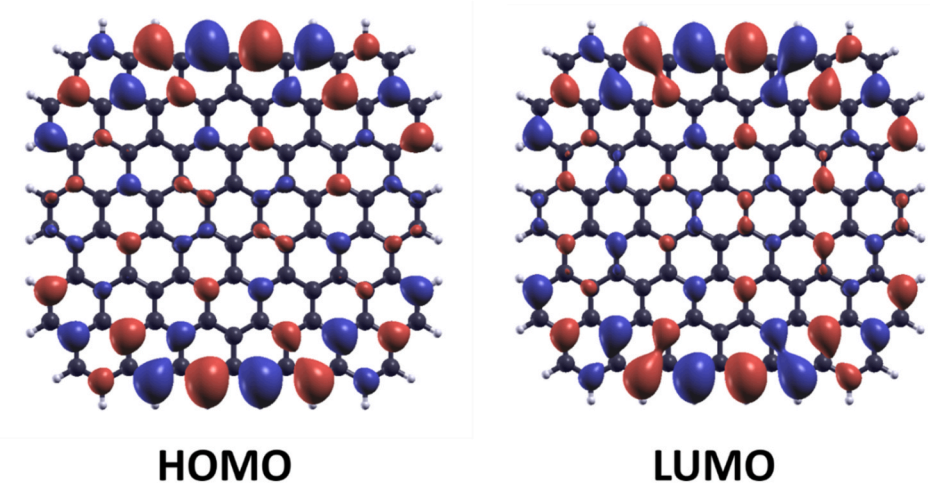

Fig. 15. Visualization of the HOMO and LUMO surface of the C_{116} CQD.

Chitosan exhibits notable impacts in acidification, climate change, and water use categories, largely due to the high energy consumption, greenhouse gas emissions, and water usage associated with its production process. In the life cycle inventory (LCI), chitosan was modelled based on the production process of chitin, sourced from crab shells. The primary environmental impacts were attributed to electricity consumption and the use of HCl and NaOH for demineralization and deproteinization, respectively. These factors significantly contribute to environmental damage which is primarily driven by the reliance on fossil fuels for electricity generation and the manufacturing of industrial chemicals. Fossil fuel usage leads to the release of harmful pollutants, posing risks such as carcinogenicity, degradation of air quality, respiratory issues, and substantial contributions to climate change. Additionally, the extensive use of HCl, NaOH, and process water generates secondary impacts, notably contributing to acidification and eutrophication in both marine and inland aquatic environments [60].

Conversely, humic acid, and citric acid display similar lower impacts, especially in the water use and human toxicity categories, suggesting potential environmental advantages associated with their use in CHFS. Specifically, citric acid holds significant promise for NCQD production, not only due to its lower environmental impact but also because it stands out in yielding NCQDs with excitation-independent emission, and higher quantum yields. This positions it as a potential frontrunner among other carbon precursors. On the other hand, Lignin presents the lowest environmental impacts in comparison to other carbon precursors, This is because of the energy efficiency of lignin extraction from kraft pulp mills, making it a preferred choice over synthetic organic compounds [61]. These findings underscore the nuanced environmental

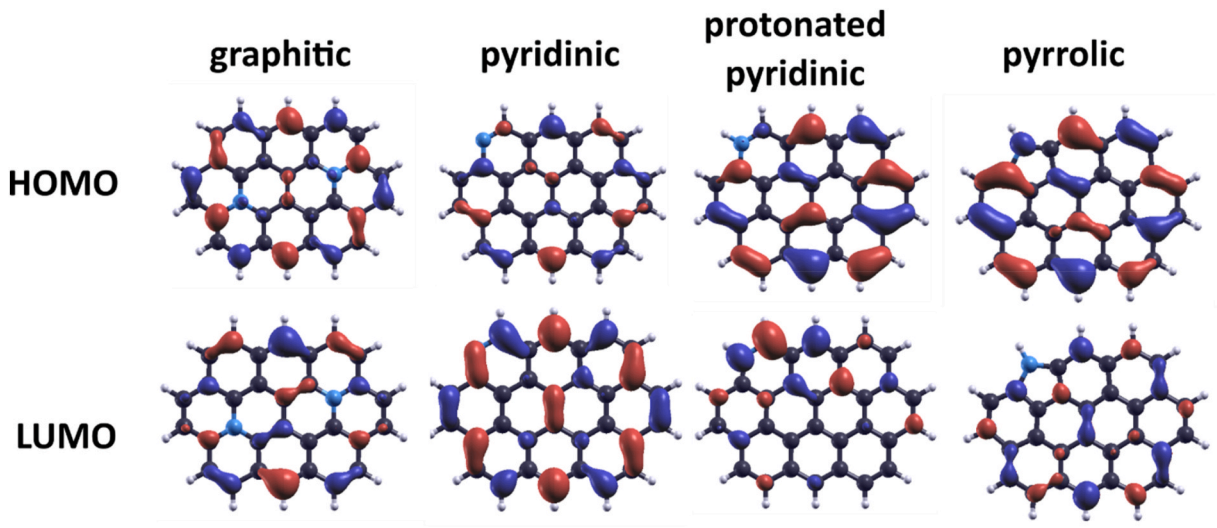

Fig. 16. Visualization of the HOMO and LUMO surface various model C_{32} NQCDs.

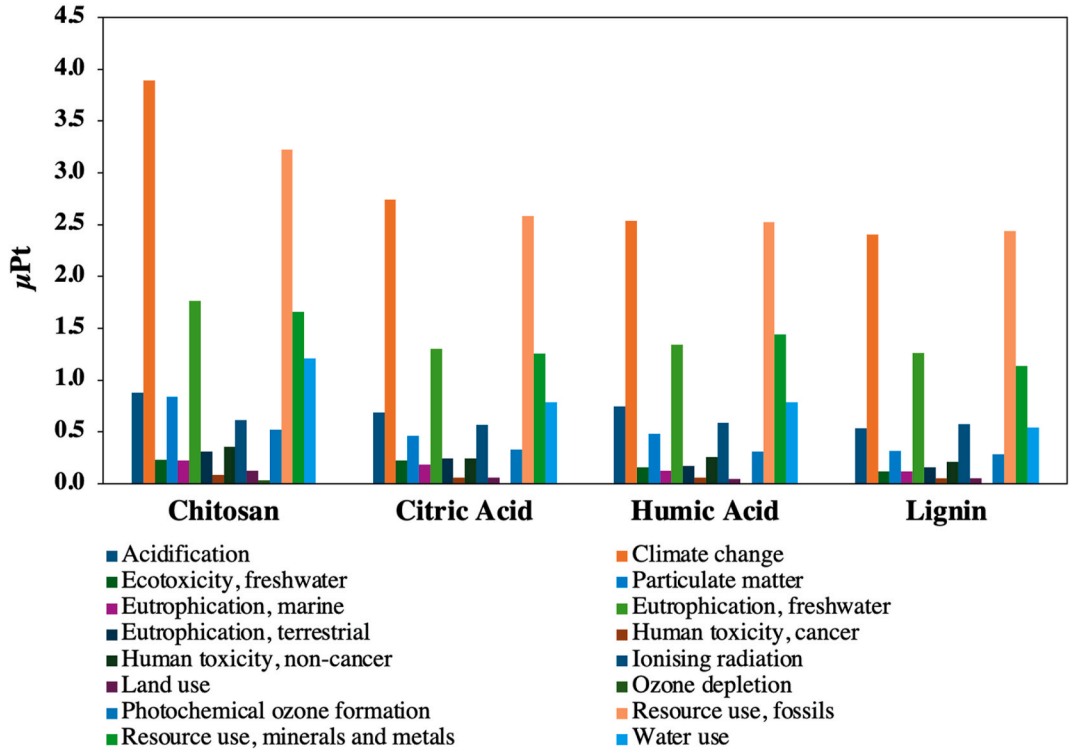

Fig. 17. Method Environmental Footprint 3.1 Version 1.00/EF normalization and weighting set/Single score – Environmental Impact assessment of CHFS using various carbon precursors to produce NQCDs.

trade-offs associated with different carbon precursors and production methods, highlighting the importance of considering sustainability implications in NCQD manufacturing processes.

In addition, selecting the appropriate precursor plays a crucial role in shaping the characteristics of the product and dictating its environmental ramifications during production. Opting for energy-intensive precursors escalates greenhouse gas emissions. Similarly, opting for inefficient precursors diminishes product yields and necessitates greater resource consumption. Hence, prioritizing sustainable and efficient precursors is imperative for mitigating the environmental impact of nanomaterials production.

In summary, the CHFS method for producing NCQDs demonstrates significantly lower environmental impacts compared to conventional Batch Hydrothermal methods (Fig. 18). Specifically, CHFS exhibits values for 'Climate Change,' 'Resource Use,' and 'Eutrophication Freshwater' that are below 20 %, whereas these same impact categories surpass 60 % in conventional Batch Hydrothermal processes. This stark contrast underscores the environmental advantages of CHFS, attributed to its continuous flow design, which enables more efficient resource utilization and minimizes emissions. Such findings highlight the potential of CHFS as a more sustainable approach for NCQDs production, offering considerable reductions in environmental burdens across key impact categories. It is important to highlight that, when normalizing the outcomes, the electricity consumption for Batch synthesis is considerably elevated compared to CHFS which arises from the extended duration of the Batch process, lasting 10 h in contrast to the

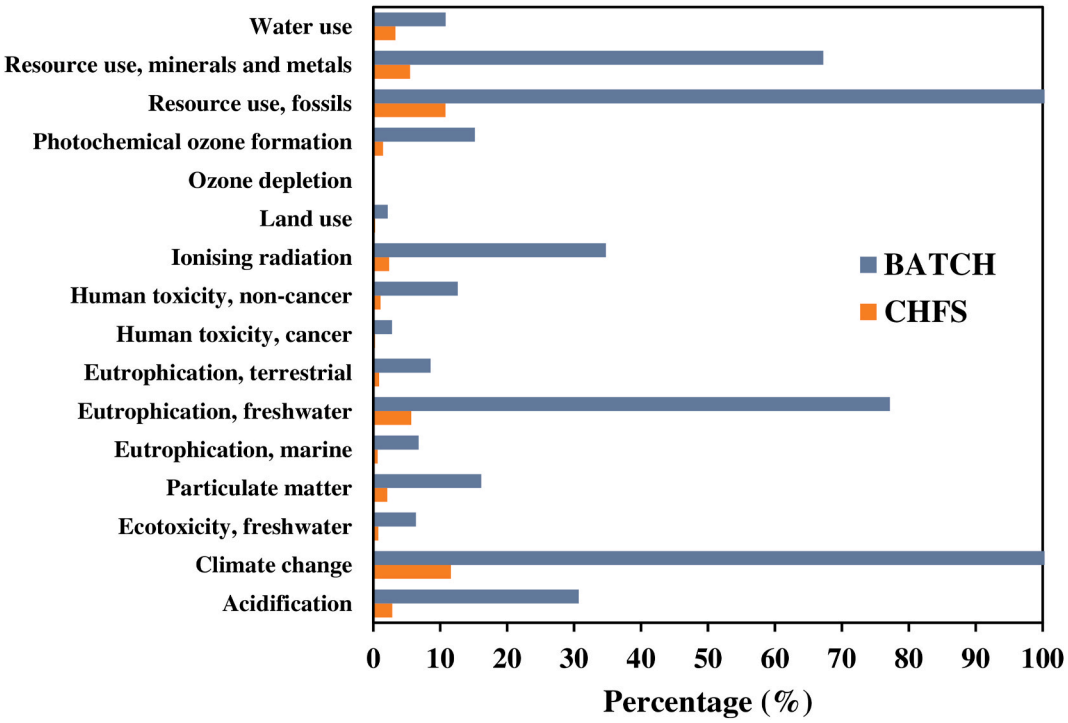

Fig. 18. Comparison of the environmental impact data for two synthesis methods (CHFS vs conventional Batch) using the same precursors to produce NCQDs. Each impact category is shown in its respective reference units, with impact scores normalized to 100 %.

rapid 10-min duration of CHFS. The electricity consumed in each process was theoretically calculated without accounting for the time taken by the CHFS reactor to reach the required reaction temperature of 450 °C, as well as the time for the furnace to reach 200 °C in Batch processes. Additionally, the power required to maintain a constant temperature during Batch processes were not considered in the calculations.

Examining the results concerning product yield for Batch synthesis, values for humic acid and lignin precursors stand at 2.37 mg mL^{-1} and 1.02 mg mL^{-1}, respectively. In contrast, utilizing the same precursors with CHFS yields significantly higher product yields of 47.96 mg mL^{-1} and 35.60 mg mL^{-1}, emphasizing the efficiency gains associated with the shorter processing time of CHFS. This disparity underscores the potential advantages of CHFS in achieving higher product yields with reduced electricity consumption compared to the lengthier Batch synthesis method.

4. Conclusion

This work demonstrates a green, rapid, and sustainable continuous hydrothermal approach for synthesizing NCQDs from various biomass-derived precursors. Leveraging the advantages of flow reactor systems enables tuneable, efficient NCQD production from a range of carbon sources such as chitosan, lignin, humic acid, and citric acid. High-resolution transmission electron microscopy (HRTEM) analysis shows that precursor structure significant impacts the size of the fabricated NCQDs, with more complex precursors tending to yield larger NCQDs. Comparing the distinct optical properties of the as-synthesised NCQDs provides key findings into their complex photoluminescence mechanisms and the role of molecular fluorophores. Citric acid stands out in producing NCQDs with excitation-independent emission, and higher quantum yield. In contrast, NCQDs derived from the polymeric precursors exhibit excitation-dependent, red-shifted, lower efficiency emission consistent with carbon core-confined states. These results highlight that the carbon source strongly influences the balance of molecular versus carbonized emitting states in NCQDs produced under same flow synthesis conditions. The optical properties of the NCQDs, including their fluorescence, depend on the particle size as well as the configuration of nitrogen dopants. Theoretical calculations show that the configuration of the nitrogen is not random. Instead, pyridinic and graphitic nitrogen atoms exhibit a strong preference to aggregate near the centre of the edge of the NCQDs and not in the vertices or the graphitic core. This is also shown to be the most active part of the NCQDs, as HOMO and LUMO are located there. Moreover, nitrogen dopants impact the work function and bandgap, thus influencing the light absorption and emission wavelengths, especially pyridinic nitrogen. The weak fluorescence exhibited by these NCQDs correlates with their limited pyrrolic nitrogen content. Furthermore, the electronic structure of the NCQDs agrees with the other characterisation results and the principles of quantum confinement effects. Therefore, this study provides molecular-level insights into the interplay between carbon sources and unique NCQDs photoluminescence mechanisms. Further, the LCA analysis highlights CHFS's green advantages for producing NCQDs over batch methods. CHFS exhibits values below 20% for climate change, resource use, and freshwater eutrophication impacts, compared to over 60% for batch hydrothermal processes. Overall, this work demonstrates the power of continuous hydrothermal flow reactors to sustainably generate NCQDs from waste biomass streams with tailored properties based on the precursor chemistry.

CRediT authorship contribution statement

Kiem G. Nguyen: Writing – original draft, Investigation, Formal analysis, Data curation. **Matej Huš:** Writing – original draft, Formal analysis, Investigation, Data curation. **Ioan-Alexandru Baragau:** Writing – review & editing, Methodology, Formal analysis. **Elisa Puccinelli:** Writing – original draft, Formal analysis, Investigation. **James Bowen:** Writing – review & editing, Formal analysis. **Tobias Heil:** Writing – review & editing, Formal analysis. **Adela Nicolaev:** Formal analysis, Writing – review & editing. **Deborah Andrews:** Writing – review & editing, Formal analysis. **Muhammad Tariq Sajjad:** Writing – review & editing, Supervision, Resources. **Steve Dunn:** Writing – review & editing, Resources. **Suela Kellici:** Writing – review & editing,

Supervision, Resources, Project administration, Investigation, Funding acquisition, Conceptualization.

Declaration of competing interest

The authors declare that they have no known competing financial interests or personal relationships that could have appeared to influence the work reported in this paper.

Acknowledgments

K.G.N., S.K. and M.T.S acknowledge the financial support provided by London South Bank University. The authors thank Dr Shaoliang Guan for his support with the UPS data collection which was performed at the EPSRC National Facility for XPS ("HarwellXPS"), operated by Cardiff University and UCL, under Contract No. PR16195. I.A.B. and A.N. would like to acknowledge the funding through the Core Program of the National Institute of Materials Physics, granted by the Romanian Ministry of Research, Innovation and Digitization through the Project PC3-PN23080303.

Appendix A. Supplementary data

Supplementary data to this article can be found online at https://doi.org/10.1016/j.carbon.2024.119623.

References

[1] A.S. Rasal, S. Yadav, A. Yadav, A.A. Kashale, S.T. Manjunatha, A. Altaee, J.-Y. Chang, Carbon quantum dots for energy applications: a review, ACS Appl. Nano Mater. 4 (2021) 6515–6541, https://doi.org/10.1021/acsanm.1c01372.

[2] A. Abbas, L.T. Mariana, A.N. Phan, Biomass-waste derived graphene quantum dots and their applications, Carbon 140 (2018) 77–99, https://doi.org/10.1016/j.carbon.2018.08.016.

[3] S. Jing, Y. Zhao, R.-C. Sun, L. Zhong, X. Peng, Facile and high-yield synthesis of carbon quantum dots from biomass-derived carbons at mild condition, ACS Sustainable Chem. Eng. 7 (2019) 7833–7843, https://doi.org/10.1021/acssuschemeng.9b00027.

[4] J. Ren, L. Malfatti, P. Innocenzi, Citric acid derived carbon dots, the challenge of understanding the synthesis-structure relationship, C, vol. 7, 2020, p. 2, https://doi.org/10.3390/c7010002.

[5] N. Abu, S. Chinnathambi, M. Kumar, F. Etezadi, N.M. Bakhori, Z.A. Zubir, S.N. Md Salleh, R.H. Shueb, S. Karthikeyan, V. Thangavel, J. Abdullah, G.N. Pandian, Development of biomass waste-based carbon quantum dots and their potential application as non-toxic bioimaging agents, RSC Adv. 13 (2023) 28230–28249, https://doi.org/10.1039/D3RA05840A.

[6] Y. Dong, L. Wan, J. Cai, Q. Fang, Y. Chi, G. Chen, Natural carbon-based dots from humic substances, Sci. Rep. 5 (2015) 10037, https://doi.org/10.1038/srep10037.

[7] A. Pundi, C.-J. Chang, Recent advances in synthesis, modification, characterization, and applications of carbon dots, Polymers 14 (2022) 2153, https://doi.org/10.3390/polym14112153.

[8] I.-A. Baragau, N.P. Power, D.J. Morgan, T. Heil, R.A. Lobo, C.S. Roberts, M.-M. Titirici, S. Dunn, S. Kellici, Continuous hydrothermal flow synthesis of blue-luminescent, excitation-independent nitrogen-doped carbon quantum dots as nanosensors, J. Mater. Chem. A 8 (2020) 3270–3279, https://doi.org/10.1039/C9TA11781D.

[9] S. Kellici, J. Acord, K.E. Moore, N.P. Power, V. Middelkoop, D.J. Morgan, T. Heil, P. Coppo, I.-A. Baragau, C.L. Raston, Continuous hydrothermal flow synthesis of graphene quantum dots, React. Chem. Eng. 3 (2018) 949–958, https://doi.org/10.1039/C8RE00158H.

[10] I.-A. Baragau, J. Buckeridge, K.G. Nguyen, T. Heil, M.T. Sajjad, S.A.J. Thomson, A. Rennie, D.J. Morgan, N.P. Power, S.A. Nicolae, M.-M. Titirici, S. Dunn, S. Kellici, Outstanding visible light photocatalysis using nano-TiO_2 hybrids with nitrogen-doped carbon quantum dots and/or reduced graphene oxide, J. Mater. Chem. A 11 (2023) 9791–9806, https://doi.org/10.1039/D2TA09586F.

[11] K.G. Nguyen, I.-A. Baragau, R. Gromicova, A. Nicolaev, S.A.J. Thomson, A. Rennie, N.P. Power, M.T. Sajjad, S. Kellici, Investigating the effect of N-doping on carbon quantum dots structure, optical properties and metal ion screening, Sci. Rep. 12 (2022) 13806, https://doi.org/10.1038/s41598-022-16893-x.

[12] I.-A. Baragau, N.P. Power, D.J. Morgan, R.A. Lobo, C.S. Roberts, M.-M. Titirici, V. Middelkoop, A. Diaz, S. Dunn, S. Kellici, Efficient continuous hydrothermal flow synthesis of carbon quantum dots from a targeted biomass precursor for on–off metal ions nanosensing, ACS Sustainable Chem. Eng. 9 (2021) 2559–2569, https://doi.org/10.1021/acssuschemeng.0c08594.

[13] K.G. Nguyen, M. Huš, I. Baragau, J. Bowen, T. Heil, A. Nicolaev, L.E. Abramiuc, A. Sapelkin, M.T. Sajjad, S. Kellici, Engineering nitrogen-doped carbon quantum dots: tailoring optical and chemical properties through selection of nitrogen precursors, Small (2024) 2310587, https://doi.org/10.1002/smll.202310587.

[14] K.P. Shejale, A. Jaiswal, A. Kumar, S. Saxena, S. Shukla, Nitrogen doped carbon quantum dots as Co-active materials for highly efficient dye sensitized solar cells, Carbon 183 (2021) 169–175, https://doi.org/10.1016/j.carbon.2021.06.090.

[15] European Chemicals Agency, RPA Europe Srl., Risk & Policy Analysts Ltd., Study on the product lifecycles, waste recycling and the circular economy for nanomaterials: November 2021, Publications Office, LU, 2021. https://data.europa.eu/doi/10.2823/708711. (Accessed 26 March 2024).

[16] A.P. Baddorf, A.J. Rondinone, D.K. Hensley, Work function measurements of clean and modified carbon nanospikes, Carbon 168 (2020) 302–307, https://doi.org/10.1016/j.carbon.2020.06.072.

[17] P. Giannozzi, O. Andreussi, T. Brumme, O. Bunau, M. Buongiorno Nardelli, M. Calandra, R. Car, C. Cavazzoni, D. Ceresoli, M. Cococcioni, N. Colonna, I. Carnimeo, A. Dal Corso, S. De Gironcoli, P. Delugas, R.A. DiStasio, A. Ferretti, A. Floris, G. Fratesi, G. Fugallo, R. Gebauer, U. Gerstmann, F. Giustino, T. Gorni, J. Jia, M. Kawamura, H.-Y. Ko, A. Kokalj, E. Küçükbenli, M. Lazzeri, M. Marsili, N. Marzari, F. Mauri, N.L. Nguyen, H.-V. Nguyen, A. Otero-de-la-Roza, L. Paulatto, S. Poncé, D. Rocca, R. Sabatini, B. Santra, M. Schlipf, A.P. Seitsonen, A. Smogunov, I. Timrov, T. Thonhauser, P. Umari, N. Vast, X. Wu, S. Baroni, Advanced capabilities for materials modelling with Quantum ESPRESSO, J. Phys. Condens. Matter 29 (2017) 465901, https://doi.org/10.1088/1361-648X/aa8f79.

[18] P. Giannozzi, S. Baroni, N. Bonini, M. Calandra, R. Car, C. Cavazzoni, D. Ceresoli, G.L. Chiarotti, M. Cococcioni, I. Dabo, A. Dal Corso, S. De Gironcoli, S. Fabris, G. Fratesi, R. Gebauer, U. Gerstmann, C. Gougoussis, A. Kokalj, M. Lazzeri, L. Martin-Samos, N. Marzari, F. Mauri, R. Mazzarello, S. Paolini, A. Pasquarello, L. Paulatto, C. Sbraccia, S. Scandolo, G. Sclauzero, A.P. Seitsonen, A. Smogunov, P. Umari, R.M. Wentzcovitch, Quantum ESPRESSO: a modular and open-source software project for quantum simulations of materials, J. Phys. Condens. Matter 21 (2009) 395502, https://doi.org/10.1088/0953-8984/21/39/395502.

[19] S. Grimme, J. Antony, S. Ehrlich, H. Krieg, A consistent and accurate *ab initio* parametrization of density functional dispersion correction (DFT-D) for the 94 elements H-Pu, J. Chem. Phys. 132 (2010) 154104, https://doi.org/10.1063/1.3382344.

[20] J.-D. Chai, M. Head-Gordon, Systematic optimization of long-range corrected hybrid density functionals, J. Chem. Phys. 128 (2008) 084106, https://doi.org/10.1063/1.2834918.

[21] S. Fazio, L. Zampori, A. De Schryver, O. Kusche, L. Thellier, E. Diaconu, Guide for EF Compliant Data Sets, Publications Office, LU, 2020. https://data.europa.eu/doi/10.2760/537292. (Accessed 4 April 2024).

[22] V. Strauss, H. Wang, S. Delacroix, M. Ledendecker, P. Wessig, Carbon nanodots revised: the thermal citric acid/urea reaction, Chem. Sci. 11 (2020) 8256–8266, https://doi.org/10.1039/D0SC01605E.

[23] Ł. Janus, M. Piątkowski, J. Radwan-Pragłowska, D. Bogdał, D. Matysek, Chitosan-based carbon quantum dots for biomedical applications: synthesis and characterization, Nanomaterials 9 (2019) 274, https://doi.org/10.3390/nano9020274.

[24] Y. Li, M. Hu, K. Liu, S. Gao, H. Lian, C. Xu, Lignin derived multicolor carbon dots for visual detection of formaldehyde, Ind. Crop. Prod. 192 (2023) 116006, https://doi.org/10.1016/j.indcrop.2022.116006.

[25] X. Liu, J. Han, X. Hou, F. Altincicek, N. Oncel, D. Pierce, X. Wu, J.X. Zhao, One-pot synthesis of graphene quantum dots using humic acid and its application for copper (II) ion detection, J. Mater. Sci. 56 (2021) 4991–5005, https://doi.org/10.1007/s10853-020-05583-6.

[26] H. Dong, M. Li, Y. Jin, Y. Wu, C. Huang, J. Yang, Preparation of graphene-like porous carbons with enhanced thermal conductivities from lignin nano-particles by combining hydrothermal carbonization and pyrolysis, Front. Energy Res. 8 (2020) 148, https://doi.org/10.3389/fenrg.2020.00148.

[27] S. Dorontić, S. Jovanović, A. Bonasera, Shedding light on graphene quantum dots: key synthetic strategies, characterization tools, and cutting-edge applications, Materials 14 (2021) 6153, https://doi.org/10.3390/ma14206153.

[28] P. Kumar, S. Dua, R. Kaur, M. Kumar, G. Bhatt, A review on advancements in carbon quantum dots and their application in photovoltaics, RSC Adv. 12 (2022) 4714–4759, https://doi.org/10.1039/D1RA08452F.

[29] A.F. Shaikh, M.S. Tamboli, R.H. Patil, A. Bhan, J.D. Ambekar, B.B. Kale, Bioinspired carbon quantum dots: an antibiofilm agents, J. Nanosci. Nanotechnol. 19 (2019) 2339–2345, https://doi.org/10.1166/jnn.2019.16537.

[30] D.W. Boukhvalov, V.Yu Osipov, D. Murzalinov, A. Serikkanov, H. Bi, A comprehensive model of carbon nanodots with 0.21 nm lattice fringes patterns, Carbon 225 (2024) 119101, https://doi.org/10.1016/j.carbon.2024.119101.

[31] K.J. Mintz, M. Bartoli, M. Rovere, Y. Zhou, S.D. Hettiarachchi, S. Paudyal, J. Chen, J.B. Domena, P.Y. Liyanage, R. Sampson, D. Khadka, R.R. Pandey, S. Huang, C. C. Chusuei, A. Tagliaferro, R.M. Leblanc, A deep investigation into the structure of carbon dots, Carbon 173 (2021) 433–447, https://doi.org/10.1016/j.carbon.2020.11.017.

[32] L. Zhu, D. Shen, K. Hong Luo, Lignin-derived carbon quantum dots-decorated $Bi_7O_9I_3$ nanosheets with enhanced photocatalytic performance: synergism of electron transfer acceleration and molecular oxygen activation, Appl. Surf. Sci. 608 (2023) 155273, https://doi.org/10.1016/j.apsusc.2022.155273.

[33] F. Lu, S. Yang, Y. Song, C. Zhai, Q. Wang, G. Ding, Z. Kang, Hydroxyl functionalized carbon dots with strong radical scavenging ability promote cell proliferation, Mater. Res. Express 6 (2019) 065030, https://doi.org/10.1088/2053-1591/ab0c55.

[34] V. Singh, S. Kashyap, U. Yadav, A. Srivastava, A.V. Singh, R.K. Singh, S.K. Singh, P. S. Saxena, Nitrogen doped carbon quantum dots demonstrate no toxicity under *in*

vitro conditions in a cervical cell line and *in vivo* in Swiss albino mice, Toxicol. Res. 8 (2019) 395–406, https://doi.org/10.1039/C8TX00260F.
[35] Y. Wang, Y. Liu, J. Zhou, J. Yue, M. Xu, B. An, C. Ma, W. Li, S. Liu, Hydrothermal synthesis of nitrogen-doped carbon quantum dots from lignin for formaldehyde determination, RSC Adv. 11 (2021) 29178–29185, https://doi.org/10.1039/D1RA05370A.
[36] Y.-J. Tong, L.-D. Yu, Y. Huang, Y. Li, N. Li, Q. Fu, Y.-X. Ye, F. Zhu, J. Pawliszyn, J. Xu, G. Ouyang, High-quality full-color carbon quantum dots synthesized under an unprecedentedly mild condition, iScience 25 (2022) 104421, https://doi.org/10.1016/j.isci.2022.104421.
[37] L.D. Movsisyan, M.D. Peeks, G.M. Greetham, M. Towrie, A.L. Thompson, A. W. Parker, H.L. Anderson, Photophysics of threaded sp-carbon chains: the polyyne is a sink for singlet and triplet excitation, J. Am. Chem. Soc. 136 (2014) 17996–18008, https://doi.org/10.1021/ja510663z.
[38] E. Dervishi, Z. Ji, H. Htoon, M. Sykora, S.K. Doorn, Raman spectroscopy of bottom-up synthesized graphene quantum dots: size and structure dependence, Nanoscale 11 (2019) 16571–16581, https://doi.org/10.1039/C9NR05345J.
[39] A. Kolanowska, G. Dzido, M. Krzywiecki, M.M. Tomczyk, D. Łukowiec, S. Ruczka, S. Boncel, Carbon quantum dots from amino acids revisited: survey of renewable precursors toward high quantum-yield blue and green fluorescence, ACS Omega 7 (2022) 41165–41176, https://doi.org/10.1021/acsomega.2c04751.
[40] A.Y. Lee, K. Yang, N.D. Anh, C. Park, S.M. Lee, T.G. Lee, M.S. Jeong, Raman study of D* band in graphene oxide and its correlation with reduction, Appl. Surf. Sci. 536 (2021) 147990, https://doi.org/10.1016/j.apsusc.2020.147990.
[41] Z. Li, L. Deng, I.A. Kinloch, R.J. Young, Raman spectroscopy of carbon materials and their composites: graphene, nanotubes and fibres, Prog. Mater. Sci. 135 (2023) 101089, https://doi.org/10.1016/j.pmatsci.2023.101089.
[42] Q. Zhang, S. Xie, Y. Yang, Y. Wu, X. Wang, J. Wu, L. Zhang, J. Chen, Y. Wang, A facile synthesis of highly nitrogen-doped carbon dots for imaging and detection in biological samples, J. Anal. Methods Chem. 2018 (2018) 1–9, https://doi.org/10.1155/2018/7890937.
[43] K. Holá, M. Sudolská, S. Kalytchuk, D. Nachtigallová, A.L. Rogach, M. Otyepka, R. Zbořil, Graphitic nitrogen triggers red fluorescence in carbon dots, ACS Nano 11 (2017) 12402–12410, https://doi.org/10.1021/acsnano.7b06399.
[44] F.A. Permatasari, R. Umami, C.D.D. Sundari, T.R. Mayangsari, A.L. Ivansyah, F. Muttaqien, T. Ogi, F. Iskandar, New insight into pyrrolic-N site effect towards the first NIR window absorption of pyrrolic-N-rich carbon dots, Nano Res. 16 (2023) 6001–6009, https://doi.org/10.1007/s12274-022-5131-7.
[45] M. Sudolská, M. Otyepka, Exact roles of individual chemical forms of nitrogen in the photoluminescent properties of nitrogen-doped carbon dots, Appl. Mater. Today 7 (2017) 190–200, https://doi.org/10.1016/j.apmt.2017.03.004.
[46] L. Sun, Y. Luo, M. Li, G. Hu, Y. Xu, T. Tang, J. Wen, X. Li, L. Wang, Role of pyridinic-N for nitrogen-doped graphene quantum dots in oxygen reaction reduction, J. Colloid Interface Sci. 508 (2017) 154–158, https://doi.org/10.1016/j.jcis.2017.08.047.
[47] T. Pillar-Little, D.Y. Kim, Differentiating the impact of nitrogen chemical states on optical properties of nitrogen-doped graphene quantum dots, RSC Adv. 7 (2017) 48263–48267, https://doi.org/10.1039/C7RA09252K.
[48] J. Song, L. Zhao, Y. Wang, Y. Xue, Y. Deng, X. Zhao, Q. Li, Carbon quantum dots prepared with chitosan for synthesis of CQDs/AuNPs for iodine ions detection, Nanomaterials 8 (2018) 1043, https://doi.org/10.3390/nano8121043.
[49] M.R. Hasan, N. Saha, T. Quaid, M.T. Reza, Formation of carbon quantum dots via hydrothermal carbonization: investigate the effect of precursors, Energies 14 (2021) 986, https://doi.org/10.3390/en14040986.
[50] W.K. Szapoczka, A.L. Truskewycz, T. Skodvin, B. Holst, P.J. Thomas, Fluorescence intensity and fluorescence lifetime measurements of various carbon dots as a function of pH, Sci. Rep. 13 (2023) 10660, https://doi.org/10.1038/s41598-023-37578-z.
[51] P. Makuła, M. Pacia, W. Macyk, How to correctly determine the band gap energy of modified semiconductor photocatalysts based on UV–vis spectra, J. Phys. Chem. Lett. 9 (2018) 6814–6817, https://doi.org/10.1021/acs.jpclett.8b02892.
[52] J. Feng, Q. Guo, N. Song, H. Liu, H. Dong, Y. Chen, L. Yu, L. Dong, Density functional theory study on optical and electronic properties of co-doped graphene quantum dots based on different nitrogen doping patterns, Diam. Relat. Mater. 113 (2021) 108264, https://doi.org/10.1016/j.diamond.2021.108264.
[53] Y. Wu, C. Li, H.C. Van Der Mei, H.J. Busscher, Y. Ren, Carbon quantum dots derived from different carbon sources for antibacterial applications, Antibiotics 10 (2021) 623, https://doi.org/10.3390/antibiotics10060623.
[54] Q. Zhang, R. Wang, B. Feng, X. Zhong, K. Ostrikov, Photoluminescence mechanism of carbon dots: triggering high-color-purity red fluorescence emission through edge amino protonation, Nat. Commun. 12 (2021) 6856, https://doi.org/10.1038/s41467-021-27071-4.
[55] S. Gavalas, A. Kelarakis, Towards red emissive systems based on carbon dots, Nanomaterials 11 (2021) 2089, https://doi.org/10.3390/nano11082089.
[56] R. Jiang, H. Wu, D. Manzani, W. Zhang, C. Liu, Effect of surface defects on photoluminescence properties of CdSe quantum dots in glasses, Appl. Surf. Sci. 622 (2023) 156931, https://doi.org/10.1016/j.apsusc.2023.156931.
[57] W. Kasprzyk, T. Świergosz, P.P. Romańczyk, J. Feldmann, J.K. Stolarczyk, The role of molecular fluorophores in the photoluminescence of carbon dots derived from citric acid: current state-of-the-art and future perspectives, Nanoscale 14 (2022) 14368–14384, https://doi.org/10.1039/D2NR03176K.
[58] Xiaoxiao Yao, Yinhan Wang, Fangjia Li, Joseph J. Dalluge, Galya Orr, Rigoberto Hernandez, Qiang Cui, Christy L. Haynes, Unconventional aliphatic fluorophores discovered as the luminescence origin in citric acid–urea carbon dots, Nanoscale 14 (26) (2022) 9516–9525, https://doi.org/10.1039/D2NR02361J.
[59] S. Morsali, Damage assessment of bitumen refineries using simapro (LCA) inventory data, J. Petrol Environ. Biotechnol. 8 (2017), https://doi.org/10.4172/2157-7463.1000317.
[60] L. Pighinelli, Methods of chitin production a short review, AJBSR 3 (2019) 307–314, https://doi.org/10.34297/AJBSR.2019.03.000682.
[61] C. Culbertson, T. Treasure, R. Venditti, H. Jameel, R. Gonzalez, Life cycle assessment of lignin extraction in a softwood kraft pulp mill, nordic pulp & paper research, Journal 31 (2016) 30–40, https://doi.org/10.3183/npprj-2016-31-01-p030-040.